

Semi-Empirical Model for Supersonic Flow Separation in Rocket Nozzles

MARCUS ALMQVIST

**MASTER OF SCIENCE PROGRAMME
in Space Engineering**

Luleå University of Technology
Department of Space Science, Kiruna



MASTER'S THESIS

Semi-empirical model for supersonic flow-separation in rocket nozzles

Carried out by

Marcus Almqvist

Master of Science program

Kiruna Space and Environment Campus, Sweden

Luleå University of Technology, Sweden

at the

Aero-thermodynamics department at Volvo Aero Corporation,
Trollhättan, Sweden

under the supervision of

Jan Östlund

Trollhättan April 2005

Abstract

The commercial potential of space flight can be described as a quotient of system performance and system weight. The system costs are primarily dependent on this quotient. To increase the quotient focus has been on reducing the system weight. After exploiting numerous ways of reducing the system weight and finally reaching the limit of mechanical load capacities, the current aim is to increase the thrust-to-weight ratio of the rocket nozzle. This is achieved by reducing the divergent length and increase the specific momentum of the nozzle, i.e. increasing the expansion ratio. However, this may causes the nozzle to be overexpanded at sea level and thus provokes the flow to separate from the nozzle wall. The unsteady and asymmetric flow separation generates lateral forces on the nozzle wall, so called side loads, which can be of dimensioning size for the nozzle and the rocket structure and not at least for the payload.

Extensive studies have been made through the years to understand the flow separation phenomena in overexpanded rocket nozzles. A better understanding could lead to better prevention or even control of flow separation. In addition, a reliable separation model is needed for accurate prediction of the side-loads experienced during start up and shut down of the engine. The aim of this thesis was to examine current separation models and try to develop a new semi-empirical model for hot gases. Focus was on the recirculation region where the flow is separated from the nozzle wall.

A new model was developed to determine the pressure- and flow distribution in the recirculation region. The model includes various parameters of the jet- and ambient gas and can therefore be used for hot gases. Several steps of the model were validated with good agreement with experimental data and numerical results found in the literature. The complete model on the other hand showed poor agreement with experiment and further work must therefore be made before the model can be useful.

Foreword

This report is submitted to the Department of Space Science in partial fulfillment of the requirements for the degree of Master of Science in Space Engineering at Luleå University of Technology, Sweden. The work was carried out at the Aero-thermodynamics department at Volvo Aero Corporation, Trollhättan.

First of all I would like to thank my supervisor Jan Östlund, for given me the opportunity to work on this project, and for the guidance and support through the work. Thanks also go to the other thesis workers at the department, Céline, Johan, Maja, Martin and Pär for making my stay at Volvo Aero a pleasant time. The supervisor of the Space Engineering program Björn Graneli and my examiner Priya Fernando also deserves a thank you for provided me with inspiration and motivation during my studies in Luleå and Kiruna. Then I would like to thank my cousin Robert Almqvist with family, the Floor ball team Sportex, and the Football team Tuns IF for making my stay in Trollhättan a pleasant time. Last but not least, I would like to thank my family who has supported me through my studies.

Contents

Abstract.....	I
Foreword.....	III
Contents	V
Nomenclature.....	VII
Abbreviations.....	VII
Symbols.....	VII
Greek letters.....	VIII
Subscripts.....	VIII
1 Introduction.....	1
2 Basic rocket knowledge.....	3
2.1 Isentropic flow.....	5
2.1.1 Area Mach number relation.....	5
2.2 Oblique shock relations.....	7
3 Full flowing supersonic nozzles.....	8
3.1 Rocket nozzles.....	8
3.1.1 The initial expansion region.....	9
3.1.2 The conical nozzle.....	9
3.1.3 Ideal nozzle.....	10
3.1.4 Truncated Ideal Contoured nozzles (TIC and CTIC).....	10
3.1.5 Thrust Optimized Contoured nozzles (TOC).....	11
3.1.6 Parabolic bell nozzles (TOP).....	12
3.2 Shock patterns in over- and underexpanded nozzle flow.....	12
4 Shock-wave turbulent boundary layer interactions.....	14
4.1 Separation criteria.....	14
4.2 Basic interactions.....	15
4.3 Free interaction theory.....	18
5 Separation in overexpanded rocket nozzles.....	19
5.1 Free shock separation FSS.....	20
5.2 Restricted shock separation RSS.....	21
5.3 Separation criteria.....	22
5.3.1 Separation criteria for FSS.....	22
5.3.2 Generalized free interaction theory.....	25
6 Semi-empirical models based on the generalized free interaction theory.....	28
6.1 Model by Reijasse & Birkemeyer.....	28
6.1.1 Flow field.....	29
6.1.2 Momentum calculations.....	29
6.1.3 Determination of the separation point.....	30
6.1.4 Results of Reijasse & Birkemeyer model.....	30
6.2 Model by Zerjeski.....	31
6.2.1 Local flow parameters and boundary layer.....	31
6.2.2 Shock and mixing layer growth.....	32
6.2.3 Momentum calculation and prediction of separation point.....	33
6.2.4 Results of Zerjeski model.....	33

6.3 Summary of the current models.....	34
7 New model for the recirculation region.....	34
7.1 Model.....	34
7.2 Isobaric jet.....	35
7.3 Nonisobaric jet.....	36
7.3.2 Continuation Isobaric jet.....	54
7.3.3. Model for “gradientless” flow in the separated zone.....	55
8 Calculations.....	55
8.1 Calculation methods.....	57
8.1.1 Calculation method 1.....	57
8.1.2 Calculation method 2.....	58
8.2 Validation.....	59
8.2.1 Validation of the Isobaric jet model.....	59
8.2.2 Validation of the geometric characteristics of an overexpanded ideal gas jet.....	62
8.3 Calculations on the nonisobaric jet model.....	66
9 Conclusion and outlook.....	70
10 References.....	72
Appendix 1 Iteration process.....	75

Nomenclature

Abbreviations

CFD	Computational Fluid Dynamics
CTIC	Compressed Truncated Ideal Contour
FSS	Free Shock Separation
LDV	Laser Doppler Velocitymetry
MOC	Method of Characteristics
RSS	Restricted shock interactions
SMME	Space Shuttle Main Engine
SWBLI	Shock-wave Boundary Layer Interactions
TIC	Truncated Ideal Contour
TOC	Thrust Optimized Contour
TOP	Thrust Optimized Parabolic Contour

Symbols

A	Area
C_f	skin friction
c	concentration of jet gas in mixing layer
c_p	specific heat
F	Force; thrust; generalized wall pressure function
g_0	9.81 [m/s ²]
H	total enthalpy
h	enthalpy; height
I	start of interaction
I_{sp}	specific impulse
i_0	H_e/H_i – dimensionless enthalpy parameter
L, l	length
M	Mach number
m	mass
\dot{m}	massflow
n	off-design pressure ratio: p_e/p_a
p	pressure
q	dynamic pressure
R	individual gas constant; reattachment point
r	radius
r_a^0	radius of ideal jet
S	separation point
T	temperature
U, u	velocity component x-dir
u_e^{**}	u_e/u_i dimensionless velocity parameter

u_e^*	$u_e/(u_i - u_e)$ dimensionless velocity parameter
u_a^0	velocity component of ideal jet
V, v	velocity component y-dir
x, y, z	cartesian-coordinates

Greek letters

α	angle
β	shock angle
δ	boundary layer thickness
δ^*	displacement thickness
δ_D	mixing layer in transformed coordinates
γ	specific heat ratio
γ_i, γ_e	adiabatic gas constant
ε	area ratio
η	efficiency; transformed coordinate
θ	wall angle
Λ	scale of turbulence
μ	ρv dynamic viscosity
μ_i, μ_e	molecular weights
ρ	density
ρ_a^0	density of ideal jet
χ	empirical constant

Subscripts

*	critical (throat) section parameters
2	point just after separation
a	ambient medium parameters
cc, 0	combustion chamber (stagnation) parameters
e	exit, outer (upper) boundary of mixing layer
i	start of interaction; inner (lower) boundary of mixing layer
max	maximum
p	plateau
r	reattachment
s	separation
sep, 1	point just before separation
t	throat, turbulent parameters
w	nozzle wall

1 Introduction

The commercial potential of space flight can be described as a quotient of system performance and system weight. The system costs are primarily dependent on this quotient. To increase the quotient focus has been on reducing the system weight. After exploiting numerous ways of reducing the system weight and finally reaching the limit of mechanical load capacities, the current aim is to increase the thrust-to-weight ratio for the rocket nozzle. This is achieved by reducing the divergent length and increase the specific momentum of the nozzle.

The optimum thrust on rocket launchers are achieved when the nozzle exit pressure is equal to the ambient pressure, i.e. an adapted or an ideally expanded nozzle.

When the exit pressure exceeds the ambient pressure, the nozzle is said to be under-expanded. The thrust loss caused by underexpansion is due to momentum loss in the outflow gas. Explained further, the high pressure gas in the nozzle is not fully expanded as it exits the nozzle, i.e. the exit gas velocity is then less than optimum, which results in a loss in thrust (momentum).

Overexpansion on the other hand arises when the exit pressure is less than the ambient pressure. The exit flow adapts to the higher ambient pressure through a shock-wave system. When the exit pressure becomes too low can the boundary layer at the wall no longer withstand the adverse pressure gradient and the nozzle flow separates from the wall. The unsteadiness of flow separation induces side loads on the nozzle wall. These side loads can be of dimensioning size for the nozzle and the rocket structure and not at least for the payload.

Sea-level launchers such as Ariane 5 and the Space shuttle are exposed to a wide span of ambient pressures while they fly through the atmosphere into space. Maximum thrust would be achieved if the nozzle could adapt its expansion ratio ϵ , i.e. adapt the exit nozzle pressure to the ambient pressure. Such a nozzle is currently not available, which provokes the nozzle to operate in off-design during most of the time of the flight (under-, overexpansion).

Extensive studies have been made through the years to understand the flow separation phenomena in overexpanded rocket nozzles. A better understanding could lead to better prevention or even control of flow separation. In addition, a reliable separation model is needed for accurate prediction of the side-loads experienced during start up and shut down of the engine.

Determination of the separation point and pressure distribution can be solved with Computer Fluid Dynamics (CFD). CFD calculations are very time consuming, and the choice of turbulence model influence the accuracy in the determination. Since it can take days or even weeks to determine the separation point and pressure distribution (with

CFD), it is desirable to find a faster method. A semi-empirical model is therefore suggested to be developed.

This paper presents the basic theory of flow separation and the existent semi-empirical models by Reijasse & Birkemeyer and Zerjeski, together with a new approach to calculate the pressure- and flow distribution in the recirculation region. The new model is a version of an integral method developed by Ginevsky, to calculate mixing layer thicknesses in turbulent mixing flows. The method takes accounts of various parameters of the jet and the ambient medium. The former two models on the other hand are only developed and tested for cold gases (air). The different gas parameters are important to include, since rocket engines operates at high temperatures with exhausts different from air.

2 Basic rocket knowledge

In combustion engines both fuel and an oxidizer is needed for the engine to work (propellant=fuel + oxidizer). Ordinary combustion engines “breathe” air and use the oxygen as an oxidizer. In comparison, rockets which operate in empty space, needs to store both fuel and oxidizer. There are two types of rocket propellants, solid and liquid. In solid propellants oxidizer and fuel are mixed together and stored in a solid face. When liquid propellants are used, fuel and oxidizer are stored separately. During operation they are injected in the combustion chamber where they are mixed and burned, see Figure 1.

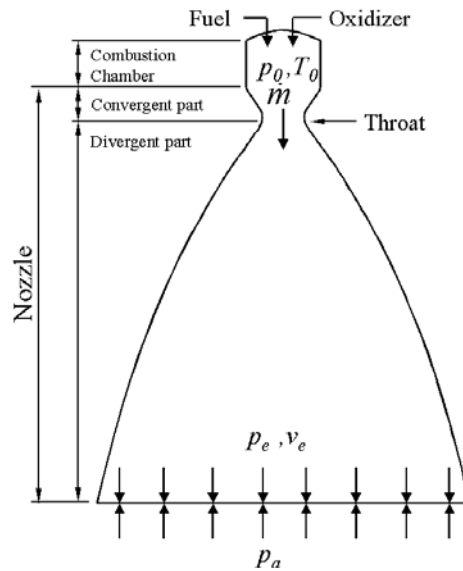


Figure 1: Characteristics of a rocket nozzle, from Östlund [1]

The basic principle driving the rocket is the famous Newtonian principle, that “to every action there is an equal and opposite reaction”. From the Newton’s second law, we know that the force on an object is equal to the change of momentum. The momentum thrust is therefore:

$$F_m = \frac{dm}{dt} v_e = \dot{m} v_e \quad (1)$$

where \dot{m} is the mass flow rate and v_e is the exit exhaust velocity of the propellant. More thrust can be generated by increasing the mass flow rate or the velocity. The mass comes from the weight of the propellants that the rocket engine expels as an exhaust gas. The combustion chamber is a constant diameter duct with sufficient length to allow complete combustion of the propellant before the nozzle accelerates the gas products. The nozzle is said to begin at the point where the chamber diameter begins to decrease.

Simply stated, the nozzle uses the stagnation temperature T_0 and stagnation pressure p_0 generated in the combustion chamber to create thrust by accelerating the combustion gas

to a high supersonic velocity. The exit velocity is governed by the nozzle expansion ratio ε , defined as the ratio between the nozzle exit area and throat area, $\varepsilon = A_e / A_t$.

In addition to the momentum thrust there are also pressure forces acting on the rocket, which leads to the following expression for the total thrust F on the rocket:

$$F = m v_e + (p_e - p_a) A_e \quad (2)$$

where p_e and A_e are the pressure and cross section area at the nozzle exit, and p_a is the ambient pressure. Another parameter that is often used to describe the efficiency of the engine is the specific impulse I_{sp} :

$$I_{sp} = \frac{F}{m} = v_e + \frac{(p_e - p_a) A_e}{m} [m/s]$$

or

$$I_{sp} = \frac{F}{m g_0} = \left(v_e + \frac{(p_e - p_a) A_e}{m} \right) / g_0 [s] \quad (3)$$

In a first glance we will expect that the highest performance will be achieved by maximize the exit pressure. But that is not the case, since the exit pressure and the exit velocity are very close and adversely coupled through the amount the nozzle expansion. This will be explained more in detail in next section. Concise, since the flow is supersonic, the velocity will increase and exit pressure will decrease as ε is increased and vice versa as ε is decreased. It can be shown that the optimum performance is obtained if the nozzle exit pressure is equal to the atmospheric pressure ($p_e = p_a$), i.e. an adapted or ideally expanded flow. This is illustrated in Figure 2, which show how the specific impulse varies with ambient pressure or flight altitude for given chamber condition equal to that of the Vulcan engine.

The solid lines show the specific impulse, the one with symbols are for nozzles with fixed expansion ratio, and the one without symbols for an adapt nozzle (able to change ε to adapt the exit pressure to the ambient pressure). The dashed line shows the corresponding expansion ratio of the adaptable nozzle. With an expansion ratio of $\varepsilon=45$, the flow becomes ideally expanded at an altitude of 10 km. From ground level up to this altitude the flow is overexpanded, i.e. $p_a > p_e$, while it is underexpanded ($p_a < p_e$) at higher altitudes.

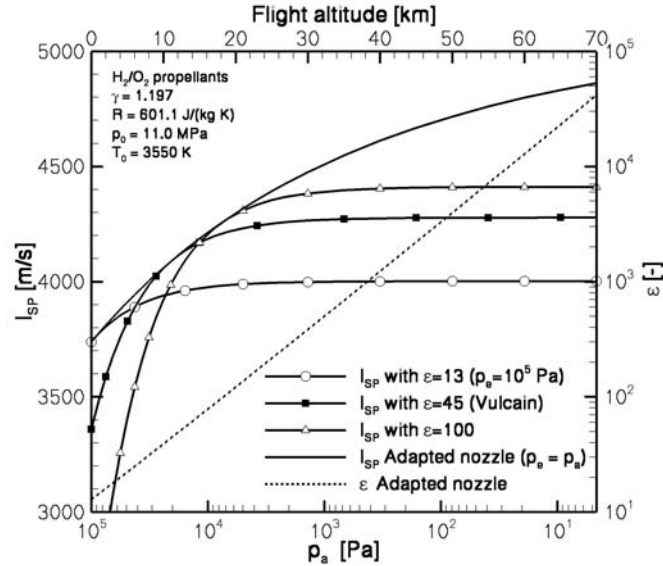


Figure 2: Performance versus pressure, from Östlund [1]

2.1 Isentropic flow

We start by introducing some definitions, from Anderson [2]:

1. Adiabatic process: one in which no heat is added to or taken away from the system.
2. Reversible process: one in which no dissipative phenomena occur, i.e. where the effects of viscosity, thermal conductive and mass diffusion are absent.
3. Isentropic process: one which is both adiabatic and reversible.
4. Perfect gas/Ideal gas: one in which intermolecular forces is neglected.

2.1.1 Area Mach number relation

As mentioned, making a complete analysis of the flow requires time consuming numerical methods, e.g. CFD. Simplified calculations can be made if the gas is assumed perfect.

Consider the nozzle in Figure 1. At the throat, the flow is sonic. By denoting the condition at sonic speed by an asterisk, we have at the throat, $M^*=1$ and $u^*=a^*$. At any other section of the nozzle, the local area, Mach number, and velocity are A , M , and u , respectively. By integrating the continuity equation over a control volume for steady flow, we will obtain:

$$\rho^* u^* A^* = \rho u A \quad (4)$$

Since $u^*=a^*$ Eq. (4) becomes

$$\frac{A}{A^*} = \frac{\rho^* a^*}{\rho u} = \frac{\rho^* \rho_0 a^*}{\rho_0 \rho u} \quad (5)$$

where ρ_0 is the stagnation density defined in Eq. (6), and is constant throughout the isentropic flow,

$$\frac{\rho_0}{\rho} = \left(1 + \frac{\gamma-1}{2} M^2\right)^{\frac{1}{\gamma-1}} \quad (6)$$

and apply this for sonic conditions, we have

$$\frac{\rho_0}{\rho^*} = \left(\frac{\gamma+1}{2}\right)^{\frac{1}{\gamma-1}} \quad (7)$$

The definition for the Mach number at the throat can be written as [2]:

$$\left(\frac{u}{a^*}\right)^2 = M^{*2} = \frac{\frac{\gamma+1}{2} M^2}{1 + \frac{\gamma-1}{2} M^2} \quad (8)$$

Squaring Eq. (5) and substituting Eqs. (6), (7) and (8), we have

$$\begin{aligned} \left(\frac{A}{A^*}\right)^2 &= \left(\frac{\rho^*}{\rho_0}\right)^2 \left(\frac{\rho_0}{\rho}\right)^2 \left(\frac{a^*}{u}\right)^2 = \left(\frac{\gamma+1}{2} M^2\right)^{\frac{2}{\gamma-1}} \left(1 + \frac{\gamma-1}{2} M^2\right)^{\frac{2}{\gamma-1}} \left(\frac{1 + \frac{\gamma-1}{2} M^2}{\frac{\gamma+1}{2} M^2}\right) \Leftrightarrow \\ &\Leftrightarrow \left(\frac{A}{A^*}\right)^2 = \frac{1}{M^2} \left[\frac{2}{\gamma+1} \left(1 + \frac{\gamma-1}{2} M^2\right)\right]^{\frac{\gamma+1}{\gamma-1}} \end{aligned} \quad (9)$$

Equation (9) is called the area Mach number relation. Turn Eq. (9) inside out, we see that $M=f(A/A^*)$, i.e. the Mach number at any location in the nozzle is function of the ratio of the local nozzle area to the sonic throat area. Equation (9) must be solved numerically. If Eq. (9) is rewritten on the form $F(M)=0$, the Euler Method (10) [4] can be used as a solver.

$$M_{n+1} = M_n - \frac{F(M_n)}{F'(M_n)} \quad (10)$$

There are two solution for every area ratio, one subsonic and one supersonic. Once the variation of Mach number through the nozzle is known, the variation of static temperature, pressure, and density is easily obtained by the following equations:

$$\frac{T_0}{T} = 1 + \frac{\gamma - 1}{2} M^2 \quad (11a)$$

$$\frac{p_0}{p} = \left(1 + \frac{\gamma - 1}{2} M^2 \right)^{\frac{\gamma}{\gamma - 1}} \quad (11b)$$

$$\frac{\rho_0}{\rho} = \left(1 + \frac{\gamma - 1}{2} M^2 \right)^{\frac{1}{\gamma - 1}} \quad (11c)$$

2.2 Oblique shock relations

The oblique shock relations describe the deflection of the flow over a shock, see Figure 3. The two angles which describe the shock are the wave angle σ and flow-deflection angle θ .

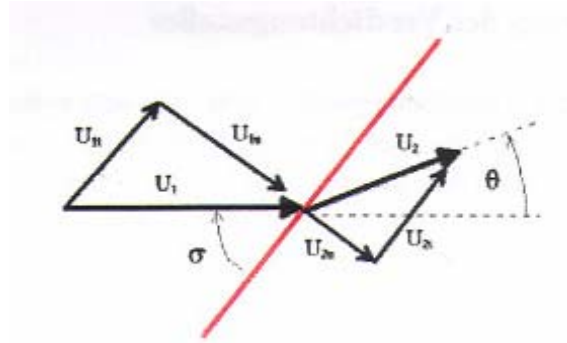


Figure 3: Oblique shock wave geometry, from [8]

It can be shown through mass conservation that the tangential velocity components are preserved over the shock, i.e. $U_{1t} = U_{2t}$. Therefore is the change over the shock governed by the normal free velocity component,

$$M_{n1} = M_1 \sin \sigma \quad (26)$$

and the following equations follow for a calorically perfect gas:

$$\frac{p_2}{p_1} = 1 + 2 \frac{\gamma}{\gamma + 1} (M_1^2 \sin^2 \sigma - 1) \quad (27)$$

$$\frac{\rho_2}{\rho_1} = \frac{(\gamma + 1)M_1^2 \sin^2 \sigma}{2 + (\gamma - 1)M_1^2 \sin^2 \sigma} \quad (28)$$

$$\frac{T_2}{T_1} = \frac{(2\gamma M_1^2 \sin^2 \sigma - (\gamma - 1))(2 + (\gamma - 1)M_1^2 \sin^2 \sigma)}{(\gamma + 1)^2 M_1^2 \sin^2 \sigma} \quad (29)$$

$$M_2^2 \sin^2(\sigma - \theta) = \frac{\gamma + 1 + (\gamma - 1)(M_1^2 \sin^2 \sigma - 1)}{\gamma + 1 + 2\gamma(M_1^2 \sin^2 \sigma - 1)} \quad (30)$$

Equation 30 can not be solved until the flow-deflection angle θ is known. By setting the tangential velocities equal and working on with some trigonometric manipulations the θ - σ -M relation can be found:

$$\tan \theta = \frac{2 \cot \sigma (M_1^2 \sin^2 \sigma - 1)}{M_1^2 (\gamma + 1 - 2 \sin^2 \sigma) + 2} \quad (31)$$

In the semi-empirical models by Reijasse & Birkemeyer and Zerjetski describes in section 6, these equation is an important part in the determination of the mixing layer.

3 Full flowing supersonic nozzles

3.1 Rocket nozzles

In the design of rocket nozzles there are several parameters that must be considered, such as performance requirements, maximum acceptable engine mass, limitations on the main dimensions, cooling performance, lifetime considerations, manufacturing methods, etc. Minimizing the weight is one of the main parameters, i.e. keeping the nozzle length and surface area at a minimum. The main gas dynamic problem lies in optimally contouring the nozzle in order to maximize efficiency. From a purely inviscid point of view, nozzles can be classified into different types, each producing its own specific internal flow field. It is essential that the designer understand these features, since the internal flow field determines the flow separation and side-load behavior. Figure 4 shows examples of the Mach number distribution in some of the most common nozzle types, which will be discussed below.

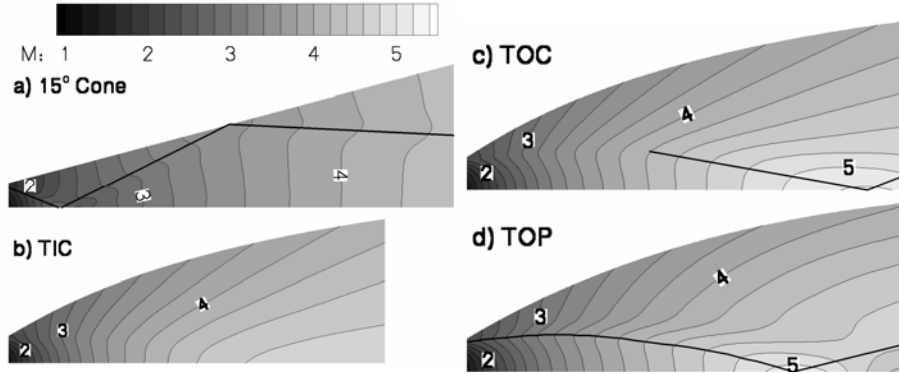


Figure 4: Mach distribution in different nozzles with $\varepsilon=43.4$. The thick line indicates the approximate position of the internal shock, [1]

3.1.1 The initial expansion region

As it turned out in Figure 4, the flow field has a more complex structure than the isentropic flow described in section 2.1.1. Currently the method of characteristics (MOC) is the most common calculation method to compute flow fields in rocket nozzles. The calculations of the flow properties downstream the nozzle is based on the kernel, which is determined by the initial expansion that occurs along the throat contour TN, which is usually designed as a circular arc, see Figure 5.

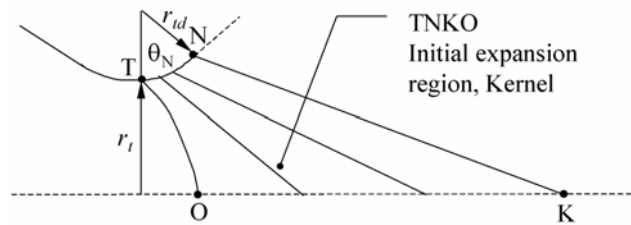


Figure 5: Initial expansion region, kernel, [1].

3.1.2 The conical nozzle

The conical nozzle has historically been the most common contour for rocket engines since it is simple and usually easy to fabricate. The exhaust velocity of a conical nozzle is essentially equal to the one dimensional value corresponding to the expansion ratio (section 2.2.1), except that the flow direction is not axial all over the exit area. Hence, there is a performance loss due to the flow divergence.

Assuming conical flow at the exit, Malina [5] showed that the geometrical efficiency is

$$\eta_{geo} = \frac{1 + \cos \alpha}{2} \quad (12)$$

where α denotes the nozzle cone half angle. The length of the conical nozzle can be expressed as

$$L_{\alpha, cone} = \frac{r_t(\sqrt{\varepsilon} - 1) + r_{td}(\sec \alpha - 1)}{\tan \alpha} \quad (13)$$

Typically, cone half angles range between 12° to 18°. A common compromise is a half angle of 15°.

Due to its high divergence losses, the conical nozzle is nowadays mainly used in short nozzles like solid rocket boosters and small thrusters, where simple fabrication is preferred over aerodynamic performance.

3.1.3 Ideal nozzle

The ideal nozzle is designed to produce an isotropic flow (i.e. a flow without any internal shocks) and a uniform exit velocity. Figure 6 describes the flow field of an ideal nozzle. After the initial section TN, the contour NE turns the flow in the axial direction. TN also defines the Mach number at K, which is equal to the design Mach number obtained at the exit. With the characteristic line NK defined and the condition that the characteristic line KE is a uniform exit characteristic it is possible to use MOC to construct the streamline between N and E, which patches the flow to become uniform and parallel at the exit.

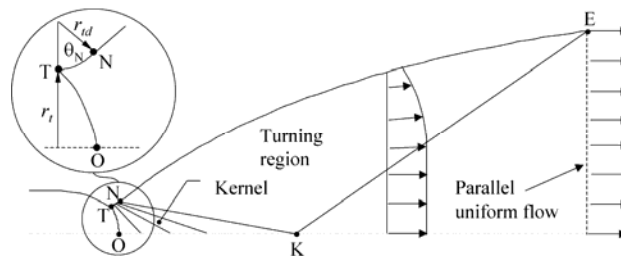


Figure 6: Basic flow structures in an ideal nozzle, [1]

3.1.4 Truncated Ideal Contoured nozzles (TIC and CTIC)

Making the exit flow uniform demands the nozzle to be very long and therefore is the ideal nozzle not suitable in rocket applications. However, since the thrust contribution in the last part of the nozzle is negligible due to the small wall slope a more effective nozzle is obtained by truncating the contour, i.e. the truncated ideal contoured nozzle (TIC). The exit velocity profile of a TIC nozzle will have a central part that is uniform and parallel, and a divergent part close to the wall, see Figure 6. The truncation can be made as far upstream as the kernel, and as long as the kernel is undisturbed can the MOC be used to calculate the flow field downstream the nozzle. Figure 4b illustrates the Mach number

distribution. An optimization technique by Ahlberg [6] is used to find the best performances for a nozzle with certain mass, surface area, exit diameter, length and thrust coefficient. TIC nozzles are for example used in the European Ariane 4 and the American Saturn-1 launcher.

A version of the TIC nozzle is the compressed TIC nozzle (CTIC). The design method of the CTIC nozzle was developed by the Japanese Gogish in the 60s. The idea is to compress a TIC nozzle linearly in the axial direction to a desired length. The compression causes the area ratio to grow faster which causes the flow to expand more rapid compared to a TIC nozzle. As a consequence, right-running compression waves will propagate from the compressed contour into the flow field. If the compression is strong enough, the characteristic lines will coalesce and form a right running oblique shock wave. If the shock wave lies near the nozzle wall, the pressure along the wall is increased and thus increasing the nozzle thrust. The CTIC nozzle is used on the Japanese H-II launcher (the LE7A nozzle).

3.1.5 Thrust Optimized Contoured nozzles (TOC)

Another design procedure for rocket nozzles today is a modified version of calculus of variables, developed by Rao [7]. The concept is; to find the exit area and nozzle contour which produces the optimum thrust for a given nozzle length and ambient pressure. The procedure can be divided into two steps. First the kernel flow (TNKO) is generated with MOC, for a variety of θ_N and a given throat curvature r_{td} , see Figure 7. Then by using calculus of variables for given design parameters (such as Mach number and area ratio or area ratio and nozzle length), the point P and N can be found by satisfying the following conditions;

1. Mass flow across PE equals the mass flow across NP.
2. The resulting nozzle gives the maximum thrust.

Once, P and N are found the kernel line NPE is fixed. The nozzle contour can then be generated by a series of parallel control surfaces P'E', P''E'' from N to P (P' and P'' are fixed on the kernel line and E' and E'' are generated), see Figure 7. As the turning of the flow (contour) are more drastic compared to an ideal nozzle (P=K) it will induce weak compression waves in the region NPE, which will coalesce into a right running shock illustrated in the Mach number distribution, Figure 4c.

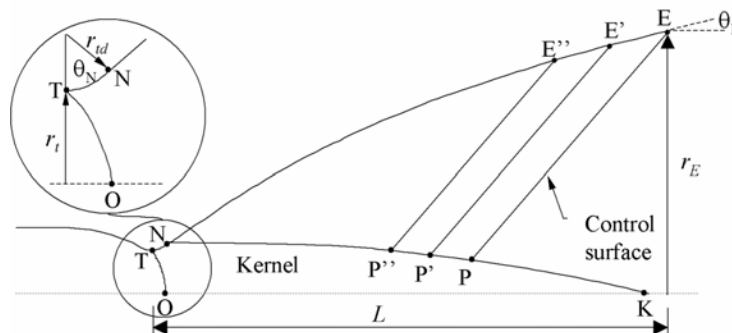


Figure 7: Thrust optimized nozzle contour, [1].

3.1.6 Parabolic bell nozzles (TOP)

Rao also developed an approximated version of the TOC nozzles, the Parabolic bell nozzles (TOP). He approximated the TOC nozzles by a skewed parabolic geometry from the inflection point to the nozzle exit.

$$\left(\frac{r}{r_i} + b\frac{x}{r_r}\right)^2 + c\frac{x}{r_r} + d\frac{r}{r_r} + e = 0 \quad (14)$$

By freely varying the five independent variables, r_{td} , θ_N , L , r_E , and θ_N , which defines the nozzle contour, any parabolic nozzle can be generated. But all of these parabolic nozzles are not a faithful approximation to a TOC, and will cause serious performance losses.

Comparing the Mach number distribution of the approximated parabolic nozzle (TOP) Figure 4d with the proposed TOC nozzle in Figure 4c it can be seen that the flow conditions along the wall are similar and that the performance is slightly less in the TOP nozzle, but there is a big difference in the shock pattern. The shock in the TOP nozzle is caused by the discontinuity in the contour at point N when the circular arc is continued with a parabolic curve. The discontinuity creates compression waves that coincide to an internal shock. This phenomenon is utilized in sea level nozzles, because it will effect the flow properties at the wall and increasing the exit wall pressure, i.e. decrease the overexpansion. The gain to reduce the overexpansion will outweigh the slight loss in performance and that's why the Vulcain 2 (used on the Ariane 5 launcher) and SSME (Space Shuttle Main Engine) are designed as TOP nozzles.

3.2 Shock patterns in over- and underexpanded nozzle flow

During flight the jet flow is ideally expanded and adapted to the surrounding flow only during a short period. The rest of the time, the rocket engine operates in off-design, i.e. the exit pressure differs from the ambient pressure. As discussed in section 2, the nozzle flow is overexpanded ($p_e < p_a$) at lower altitudes than design altitude, and underexpanded ($p_e > p_a$) at higher altitudes than design altitude. When the rocket engine operates in off-design, compression and expansion waves are formed around the exhaust jet, with consequent density discontinuities, which gradually achieve a match between the pressure in the jet and the ambient pressure. The Pressure ratio n (15) is often used to describe the off-design supersonic discharge.

$$n = \frac{P_e}{P_a} \quad (15)$$

An illustration of the exhaust plume patterns at underexpanded ($n > 1$), adapted ($n = 1$) and at overexpanded (but not separated flow) condition ($n < 1$) is given in Figure 8.

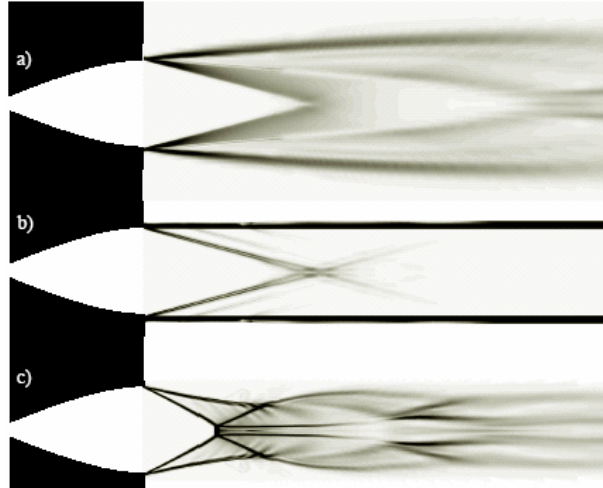


Figure 8: Flow patterns behind the nozzle, a) Under- ($p_e/p_a=2$), b) Ideal ($p_e/p_a=1$) and c) Over- ($p_e/p_a=0.3$) expanded flow, [1]

Figure 9 shows photographs on nozzle exhaust flows in off-design. In overexpanded flows, different barrel-like exhaust plumes can be formed when the exhaust flow adapts to the ambient flow through a system of oblique shocks and expansion waves. The different plume patterns are presented in Figure 9, the classical Mach disc, Figure 9a, the cap-shock pattern, Figure 9b and the apparent regular shock reflection at the centerline, Figure 9c. Figure 9d illustrate a Saturn 1-B rocket in underexpanded condition, resulting that the flow continues to expand behind the rocket. The actual shape of the overexpanded shock pattern depends on the nozzle contour type (internal flow field) and degree of overexpansion.

In ideal and TIC nozzles, a transition between the Mach disc and the apparent regular shock reflection is a matter of overexpansion. When the overexpansion is small, the flow is able to adapt to the ambient pressure without forming a strong shock system, i.e. a Mach disc.

The cap shock can only be observed in nozzles with an internal shock, i.e. TOC, TOP and CTIC nozzles. The cap shock is observed at the nozzle exit during start up. When the combustion pressure increases the flow becomes less overexpanded. At some point the internal shock intersects the centerline and a transition to a Mach disc pattern takes place. The shock patterns described above are not only exhausting plumes, they also exist inside nozzles at highly overexpanded flow conditions, when the flow is separated from the wall.

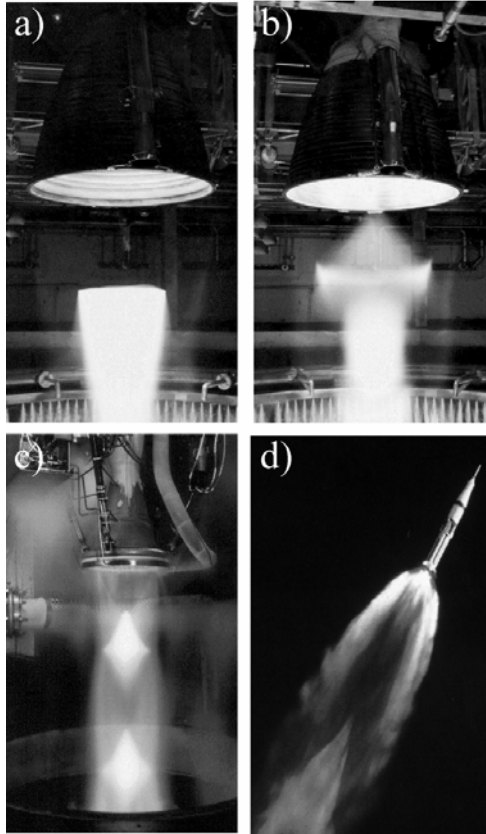


Figure 9: Exhaust plume patterns, [1]

4 Shock-wave turbulent boundary layer interactions

As mentioned in the previous section, when a supersonic flow is exposed to an adverse pressure gradient it adapts to the higher pressure level through a shock wave system. The complex unsteady and three dimensional phenomena that are created between the separated jet and the shock are called, Shock Wave Boundary Layer Interactions (SWBLI).

4.1 Separation criteria

1904 formulate Prandtl for the first time the stationary ($\frac{\partial}{\partial t} = 0$) Boundary Layer Equations ((16)-(18)). Due to no slip condition, the velocity on the surface of a stationary body is zero, which simplifies the momentum and continuity equation to the following form:

Momentum equation:
$$u \frac{\partial u}{\partial x} + v \frac{\partial u}{\partial y} = -\frac{1}{\rho} \frac{\partial p}{\partial x} + \nu \frac{\partial^2 u}{\partial y^2} \quad (16)$$

Continuity equation:
$$\frac{\partial u}{\partial x} + \frac{\partial v}{\partial y} = 0 \quad (17)$$

with
$$\frac{\partial p}{\partial y} = 0 \quad (18)$$

Basically, separation occurs at the point where the turbulent boundary layer no longer can withstand the adverse pressure gradient imposed upon it by inviscid outer flow. The criterion for separation is defined as the limit between forward and reverse flow in the immediate neighborhood of the wall, i.e. the point where $\left(\frac{\partial u}{\partial y}\right)_{y=0} = 0$, which simplifies Equation (16)

$$\frac{1}{\rho} \frac{\partial p}{\partial x} = \nu \frac{\partial^2 u}{\partial y^2}, \text{ at } y=0. \quad (19)$$

The velocity profile and the separation point are illustrated in Figure 10. As a note, separation can only occur when the potential flow is retarded, i.e. $\frac{dp}{dx} > 0$.

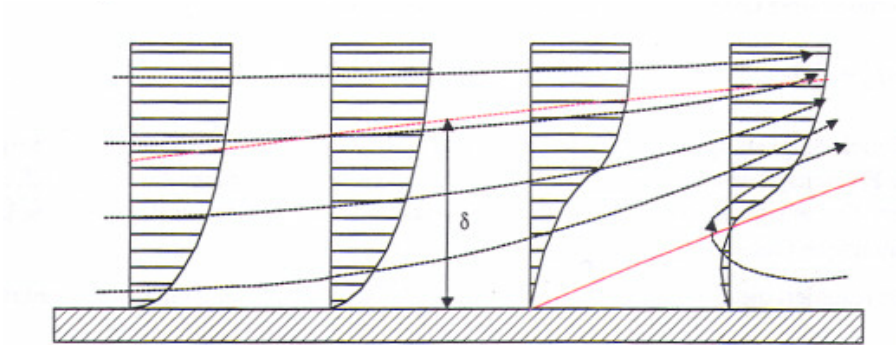


Figure 10: Velocity profile at the separation point, from Zerjeski [8]

4.2 Basic interactions

During the last 50 years the volition to understand the phenomena of shock wave boundary layer interaction has lead to extended studies through experiments. The work has been focused on three different configurations that involve interaction between a shock wave and a turbulent boundary layer in supersonic flow. These configurations are illustrated schematically in Figure 11. Before the interaction the incoming flow is a uniform flow along a plate.

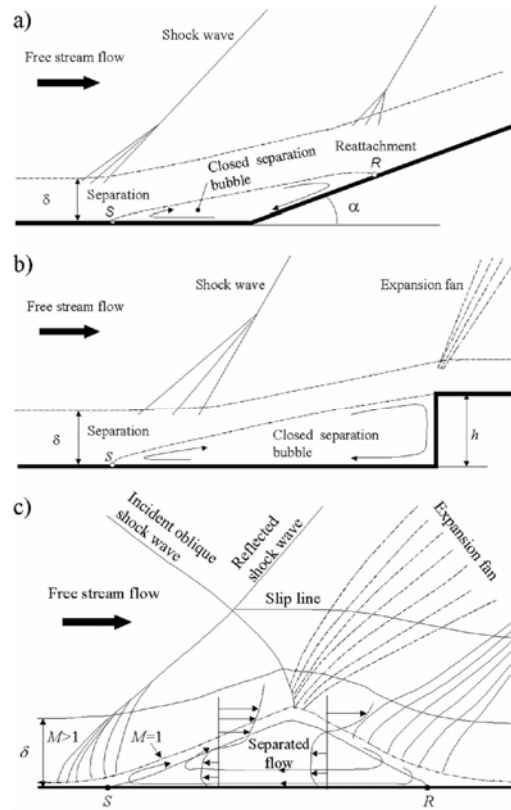


Figure 11: Basic shock/boundary layer interactions in supersonic flow. a) Ramp flow, b) Step induced separation c) Shock reflection

The first configuration is the wedge (or ramp) flow, Figure 11a. The incoming uniform flow undergoes a deflection equal to the ramp angle α . For small angles ($\alpha < 15^\circ$) can the deflection occur without any separation. But when the deflection angle becomes too big, the pressure rise forces the boundary layer to separate from the wall and creates a separation bubble. Two shocks are formed; the first at the separation point and the other at the reattachment point. The two shocks coincide downstream the flow in an oblique shock.

The second type is separation induced by a step of height h facing the flow, see Figure 11b. The step decreases the supersonic flow and gives raise to a sudden pressure rise. The boundary layer separates from the wall at the separation point S, and induces a shock wave starting near the separation point. Between the separation point and the step is a separation zone created.

The third type is separation caused by impingement of an oblique shock on a smooth wall, Figure 11c. The incident shock causes a deflection of the incoming flow, and a reflected shock is formed, as the downstream flow tends to become parallel to the wall.

Performed experiments on these three types have shown that the upstream part of interaction between the shock and the boundary layer is nearly independent of cause of separation, whether it is a solid obstacle or an incident shock wave. It has also been shown that the static wall pressure illustrated in Figure 12 has the same shape, independent of separation type. The wall pressure has a step rise short after the beginning

of the interaction at I. The flow separates from the wall at point S, located at a distance L_s from I. If the separated flow scale is large enough, the wall pressure then gradually approaches a plateau with almost constant pressure, labeled the plateau pressure p_p . A second pressure rise can be observed as the reattachment point at R is approached. These characteristics are independent on the downstream geometry, everything happens as if the flow were entirely determined by its properties at the onset of the interaction.

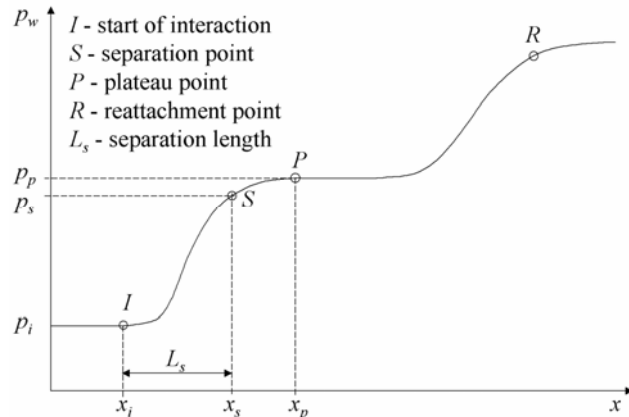


Figure 12: Typical static wall pressure distribution.

The pressure distribution above, illustrate the mean (static) pressure in the separation region. There is also a dynamic pressure, illustrated in Figure 13. The dynamic arise due to fluctuating of the separation point which causes the pressure to fluctuate between the pressure p_i at the incipient point and the plateau pressure p_p . Upon that there are also the slightly pressure variation at x_i and x_p (p_i' and p_p').

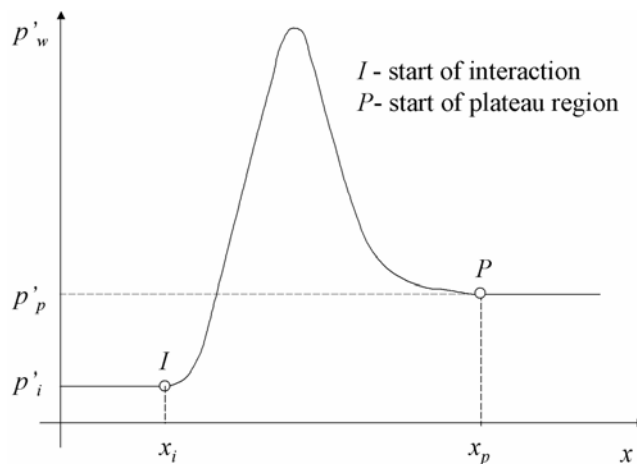


Figure 13: Typical distribution of the fluctuating pressure in the interaction region near separation.

4.3 Free interaction theory

The observations that the wall pressure distribution has the same shape independent of origin of separation, lead Chapman *et al.* [9] to formulate a theory of free interaction. The theory was formulated to be applied in a case of plan, adiabatic, supersonic uniform flow, to compute the pressure distribution caused by boundary layer – shock interactions. As mentioned above, the flow is determined by its properties at the onset of the interaction. Therefore are, the Mach number M_i and the pressure p_i defining the inviscid uniform flow. The skin friction coefficient (C_f), the displacement thickness (δ^*) etc. define the local characteristics of the boundary layer. The deflection of the mean flow in the streamwise direction is called θ . Figure 14 illustrate the schematic flow field.

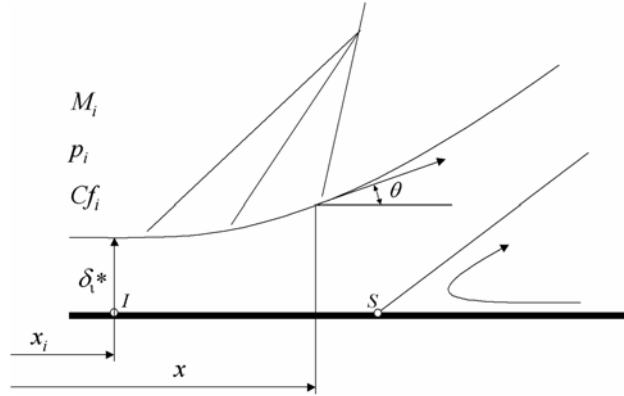


Figure 14: Flow separation in uniform flow, notations [1].

Chapman *et al.* made two assumptions about the flow in the interaction region:

1. The flow structure follows a law of similarity
2. The deviation of the external non-viscid flow corresponds precisely to the displacement effect of the boundary layer:

$$\frac{d\delta^*}{dx} = \theta - \theta_i. \quad (20)$$

The corner stone in the free interaction theory is the boundary layer momentum equation at the wall:

$$\frac{\partial p_w}{\partial x} = \frac{\partial \tau_w}{\partial y} \quad (21)$$

By integrating this equation from $x=x_i$, Chapman found a generalized form to write the streamwise pressure distribution,

$$F(s) = \sqrt{\frac{p - p_i}{q_i} \frac{v(M_i) - v(M)}{C_{f_i}}} \quad (22)$$

where $s=(x-x_i)/l$, l is a reference length characterizing the extent of the domain, q_i is the dynamic pressure (Eq. 23), v is the Prandtl- Mayer function (Eq. 24), and C_{fi} is the skin friction coefficient at the point I.

$$q_i = \frac{1}{2} \gamma p_i M_i^2 \quad (23)$$

$$v = \sqrt{\frac{\gamma+1}{\gamma-1}} \arctan \sqrt{\frac{\gamma-1}{\gamma+1} (M^2 - 1)} - \arctan \sqrt{M^2 - 1} \quad (24)$$

Chapman then expressed the variation of $v(M_i) - v(M)$ as a function of $(p - p_i)/q_i$, linearised it for small pressure changes $p - p_i$ and obtained

$$F(s) = \frac{p - p_i}{q_i} \sqrt{\frac{\sqrt{M_i^2 - 1}}{2C_{fi}}}. \quad (25)$$

$F(s)$ is determined from experiments and is assumed to be a universal function, independent of Mach number and Reynolds number. Erdos & Pallone [10] determined the generalized wall pressure correlation function $F(s)$, presented in Figure 15.

They used $l=L_s=x_f-x_s$ as a reference length, where x_i, x_s are the onset of the interaction and separation length respectively. From Figure 15 it can be found that the correlation function $F(s)$ has the following fixed value, $F_s=F(1)=4.22$ at the separation point and $F_p=F(4)=6$ at the plateau point x_p .

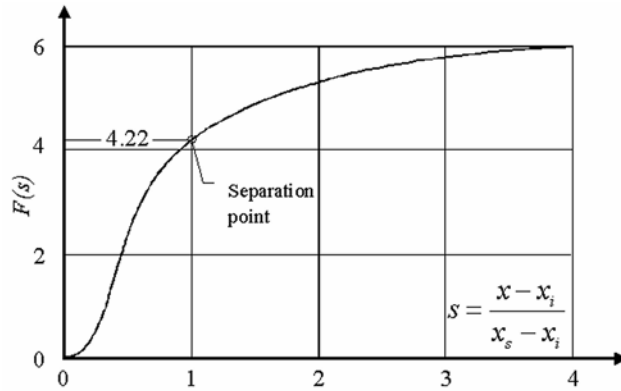


Figure 15: Generalized wall pressure correlation function $F(s)$ for uniform turbulent flow, by Erdos & Pallone [10].

5 Separation in overexpanded rocket nozzles

The previous chapter treated the general concept of shocks and separation of boundary layers from walls, when the uniformed flow was exposed to adverse pressure gradient. The exhaust jet from rocket nozzles which operate in overexpansion ($n < 1$) is exposed to a similar pressure gradient. Overexpansion occurs when the rocket nozzle is exposed to a

higher ambient pressure than the design pressure, and also during start up transient, shut down transient, or engine throttling modes. As soon as n slightly is reduced below unity, an oblique shock system is formed at the exit of the nozzle (sec. 3.2). When n is reduced further to a level about 0.4-0.8, the viscous layer can no longer sustain the adverse pressure gradient imposed upon it by the inviscid flow and the boundary layer separates from the wall.

Research has shown that there are at least two different separation patterns inside the nozzle, the classical free shock separation (FSS) and the restricted shock separation (RSS).

5.1 Free shock separation FSS

Free shock separation is when the flow is fully separated from the wall, i.e. the flow is separated from the beginning of the interaction throughout the nozzle. In Figure 16, the FSS pattern together with its characteristic points is illustrated. As mentioned earlier, the separation of the flow occurs when the overexpansion becomes too big. As the overexpansion grows (n decrease), the separation point moves further upstream the nozzle and vice versa as the overexpansion decreases.

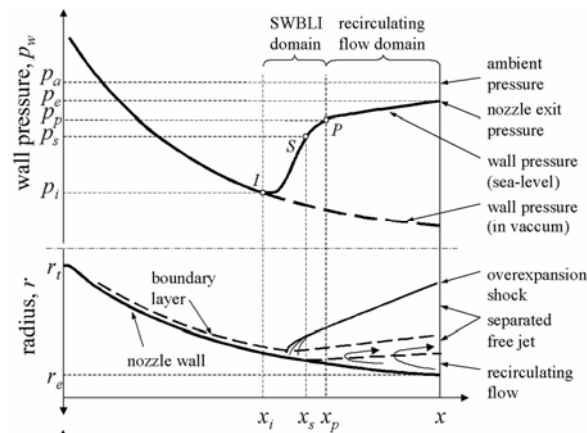


Figure 16: Illustration of free shock separation, [1].

By studying the pressure pattern in Figure 16 we see that the flow can be divided into three regions. First; upstream the incipient point (x_i), where the boundary layer is attached to the wall and has the same behavior as a full throttled nozzle. Second; the region there the pressure rises from minimum pressure (p_i) to the plateau pressure (p_p) ($x_i < x < x_p$). This region is referred as the separation- or the interaction- or the intermittent region. The boundary layer starts to be deflected at the incipient point (x_i), but it does not separate from the wall until the friction force τ_w is zero, at the separation point x_s . In the third and last region referred as the recirculation region the flow is fully separated. When the jet flow separates from the wall, the jet gas is replaced by ambient gas in the recirculation region. As the recirculation region becomes narrower upstream the nozzle, the ambient gas accelerates and therefore causes the pressure to slightly decrease. This causes the slightly pressure increment from the plateau pressure (p_p) at x_p to exit pressure

(p_e) at the nozzle exit (almost ambient pressure). Figure 17 shows a CFD calculation of the Mach number distribution.

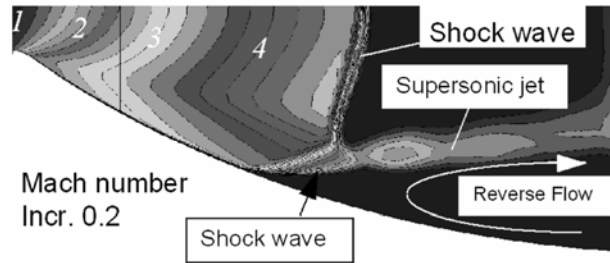


Figure 17: Calculated Mach number distribution in Volvo S1 nozzle ($n=0.13$), [1].

5.2 Restricted shock separation RSS

The other pattern is the restricted shock separation, which was discovered for the first time during cold gas tests of the J-2S nozzle in the early 70s. The RSS pattern of the flow field and pressure distribution is illustrated in Figure 18.

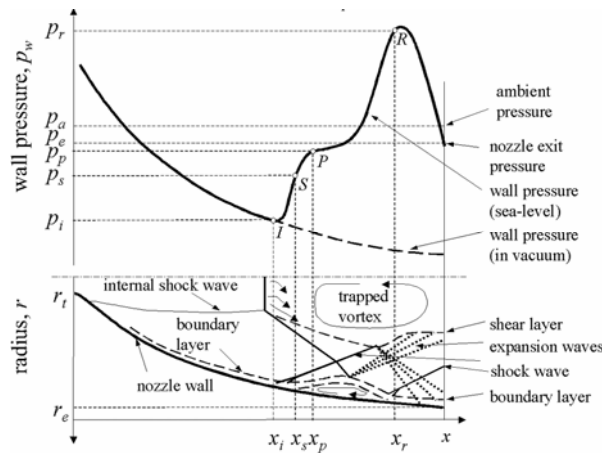


Figure 18: Illustration of restricted shock separation, [1].

It can be seen that the shock pattern are similar to the pattern for an incident oblique shock wave described in section 4.2 (Figure 10). The RSS pattern only occurs in strongly overexpanded nozzles with an internal shock (TOP, CTIC). The pattern arises when the flow separates (deflects) from the wall and forms a shock wave, due to the overexpansion. The deflected flow is then reflected towards the wall by the shock aroused from the cap shock. If the reflection is sufficient strong, it will cause the flow to be reattached to the wall, which forms a closed separation bubble. The difference in pressure pattern for RSS and FSS is that the RSS pressure pattern rises from the plateau pressure (p_p) at x_p towards the maximum pressure (p_r) at the reattachment point x_r . Figure

19 illustrates a CFD (numerical) calculation of the Mach number distribution for a free shock separation.

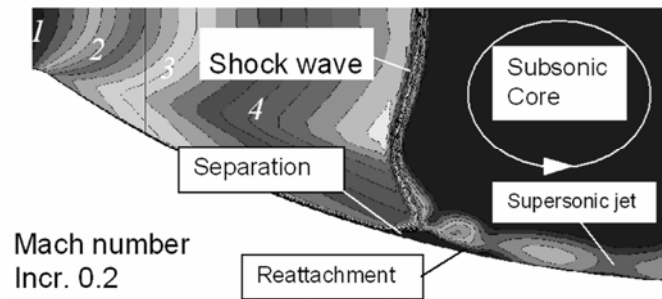


Figure 19: Calculated Mach number distribution in Volvo S1 nozzle ($n=0.15$), [1]

5.3 Separation criteria

As mentioned in the introduction, predictions of the separation point and the pressure distribution along the nozzle wall are prerequisite before a reliable side load model can be made. For instance in nozzles featuring transition between FSS and RSS, the “worst case” side-load occurs when one half of the nozzle experience RSS and the other half FSS [1]. Extended studies and experiments have been performed on overexpanded rocket nozzles in an attempt to understand and predict the flow separation better. Most of the studies are performed on conical and truncated ideal nozzles which only feature free shock separation. The extended studies have resulted in a number of empirical and semi-empirical models to predict the separation point. It should be noted that the separation point fluctuates between two extremes. Due to the wide spectrum of parameters in the boundary layer- shock interaction (e.g. nozzle contour, gas properties, wall temperature, wall configuration and roughness) no reliable separation point model is available today. Some of the current separation point models for FSS are presented below.

5.3.1 Separation criteria for FSS

The most simple and classical criteria for FSS was formulated by Summerfield *et al.* [11], which is purely based on extensive experiments from conical nozzles in the late 1940s.

$$\frac{p_i}{p_a} \approx 0.4 \quad (32)$$

Schilling [12] derived 1962 a simple empirical model based on experiments from conical and truncated ideal nozzles. The model was accounting for the increase of separation pressure ratio p_i/p_a with increasing Mach number,

$$p_i/p_a = k_1(p_0/p_a)^{k_2} \quad (33)$$

with $k_1=0.582$ and $k_2=-0.195$ for contoured nozzles, and $k_1=0.541$ and $k_2=-0.136$ for conical nozzles. But the model has one big weakness; the separation ratio p_i/p_p is higher for cold gas nozzles than for hot gas nozzles, and that's the opposite what the experiments in the literature shows.

The first semi-empirical criterion was derived by Crocco & Probstein [13], which is based on a simplified boundary layer integral approach. The criterion accounts for properties of the boundary layer, the gas and the inviscid Mach number at the onset of the separation. The criterion showed a variation of agreement with experimental data. NASA therefore recommended a 20% margin to the predicted separation point (1976). At the same time Schmucker [14] derived the empirical criterion

$$p_i/p_a = (1.88M_i - 1)^{-0.64} . \quad (34)$$

Despite its simplicity it shows a similar agreement with experimental data as the Crocco & Probstein criterion, and is therefore still widely used.

The rather poor agreement of the above criteria can be explained by studying Figure 16. The pressure rise in the above criteria is described with one expression that are involving two mechanism, the pressure rise near the separation point and the slightly pressure rise in the recirculation area. Lawrence [15] therefore suggested that the pressure ratio p_i/p_a should be subdivided into two parts $p_i/p_p \cdot p_p/p_a$, and described separately. The pressure ratio p_i/p_p is caused by the shock-wave boundary layer interaction described in section 4.

Zukoski [16] described the pressure ratio p_i/p_p at the simple form

$$\frac{p_i}{p_p} = \frac{2}{2 + M_i} . \quad (35)$$

The criterion shows good agreement with performed experiments. But it has the drawback that all experiments were performed with air, and thus does not include the dependency of specific heat γ .

Östlund [17] has developed a criterion for the pressure ratio p_i/p_p , which is based on oblique shock relations.

$$\frac{p_i}{p_p} = \left\{ 1 + \gamma M_i^2 \sin^2(\beta) \left[1 - \frac{\tan(\beta - \theta)}{\tan(\beta)} \right] \right\}^{-1} \quad (36)$$

with $\beta = -3.764M_i + 42.878$ [°] and $\theta = 1.678M_i + 9.347$ [°] for Mach number range $2.5 \leq M_i \leq 4.5$. Frey [18] has proposed a similar criterion based only on the shock angle β ,

$$\frac{p_i}{p_p} = \left[1 + \frac{2\gamma}{\gamma+1} (M_i^2 \sin^2(\beta) - 1) \right]^{-1} \quad (37)$$

with $\beta = -4.7M_i + 44.5$ [°] for Mach number range $2.5 \leq M_i \leq 4.5$.

The discovery that the pressure rise should be subdivided into two parts resulted in a better agreement with performed experiments. The above criteria are quite simple and purely empirical, and are not built on a physical model which would be favorable to describe the pressure rise correctly. A promising theory which includes the physics in the separation region is the generalized free interaction theory by Carrière [19]. This criterion will be discussed separately in next section, due to its importance in current semi-empirical models for flow separation in overexpanded nozzles.

To be able to describe the pressure distribution throughout the nozzle a criterion for the pressure ratio p_p/p_a is also needed. Today there are no such models available for contoured nozzles operated with hot gases, but there are two models available for conical nozzles operated with air, one by Kudryavtsev [20] and one by Malik & Tagirov [21]. The one by Kudryavtsev is purely empirical for half angles $\alpha < 15^\circ$,

$$\frac{p_p}{p_a} = \left[1 + \left(\frac{0.192}{\sin \alpha} - 0.7 \right) \left(1 - \frac{M_i}{M_a} \right) \right]^{-1} \quad (38)$$

where M_a is the average exit Mach number defined by the nozzle expansion ratio ε . For $\alpha > 15^\circ$, he found out that pressure ratio $p_p/p_a \approx 1$, i.e. independent of the Mach number.

The one by Malik & Tagirov is semi-empirical and have showed good agreement with test data, see Figure 20. The model is based on Abramovich's theory for mixing of counter flowing turbulent jets. Generalizing of this model to contoured nozzles operated with hot gases could be a promising model in the future to describe the recirculation flow.

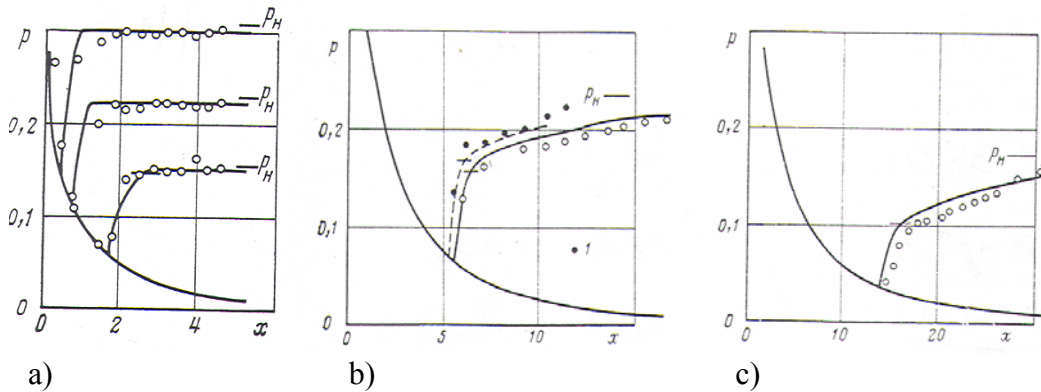


Figure 20: Calculated and experimental pressure distributions for different conical nozzles, a) $\alpha = 22.5^\circ$, b) $\alpha = 7^\circ$, and c) $\alpha = 4^\circ$, from Malik & Tagirov [21]

5.3.2 Generalized free interaction theory

As mentioned in section 4.3, the free interaction theory of Chapman can be applied for uniform supersonic flows to calculate the pressure distribution due to the boundary layer-shock interaction. This theory has been generalized by Carrière [19] for non-uniform incoming flows as well as the curvature in the interaction region. The non-uniformity of the flow is by Carrière described with a normalized pressure gradient in the axial direction

$$p' = \frac{\delta_i^*}{q_i} \frac{dp}{dx} \quad (39)$$

where δ_i^* is the displacement thickness at the beginning of the interaction. In the most generalized case, the universal wall pressure correlation function (Eq. 22) can be rewritten for non-uniform flows on the form:

$$F\left(\frac{x-x_i}{x_s-x_i}, p'\right) = \sqrt{\frac{p(x)-p_i(x)}{q_i} \frac{\bar{v}(x)-v(x)}{C_{fi}}} \quad (40)$$

where v is the Prandtl-Meyer function for the actual pressure at x and \bar{v} the value v would take at the same location in absence of flow separation. The Mach number in the Prantl-Mayer function (Eq. 24) can be found from the isotropic relation (Eq.11b)

$$M = \sqrt{\frac{2}{\gamma-1} \left[\left(\frac{p}{p_0} \right)^{\frac{1-\gamma}{\gamma}} - 1 \right]} \quad (41)$$

Substituting Eqs. (41) and (24) into (28), it can be realized that the correlation function F is independent of the Mach number and Reynolds number. The correlation function F was determined by Carrière through experiments on one ideal nozzle and three conical nozzles. Figure 21 shows the generalized pressure correlation function F and the separation length l_s . The uniform flow correlation function is also included in the figure as a comparison.

The next step is to define the value of the correlation function F at the separation point x_s and/or the plateau point x_p . Carrière suggested to use the separation point in his further calculations and therefore defined $F=F_s=4.22$. Östlund on the other hand suggested using the plateau point x_p and defined $F=F_p=6$, which is analogous to Erdos & Pallone's definition of the plateau point for uniform flows.

In Equation 40 there is still one variable that is unknown, the interaction length l_s (l_p). To find an interaction length law (ILL), least square methods were used by fitting experimental pressure distributions to a theoretical curve, see Figure 21b.

When x_i and x_p (x_s) are determined/assumed (explained further in next section), Equation (40) becomes an implicit system with one variable (x) and must therefore be solved iteratively, e.g. with the Euler method (10)

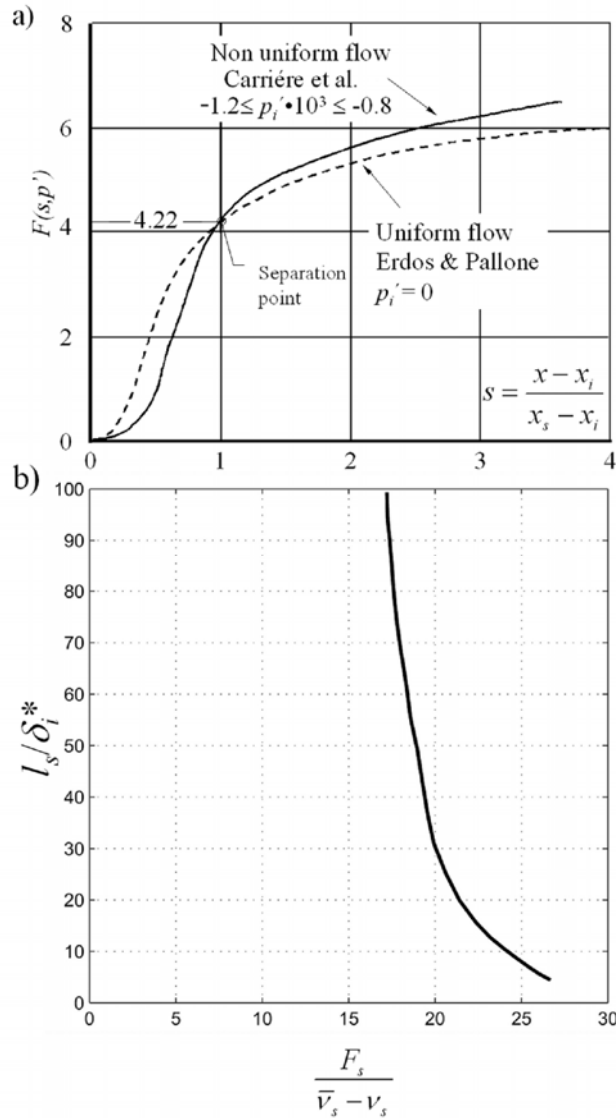


Figure 21: a) Wall pressure correlation, and b) separation length for $F_s=4.22$, according to the generalized free interaction theory for non-uniform flow by Carrière [19]

Östlund suggested a method to determine the start of the interaction point (x_i), if the nozzle operation condition and plateau pressure were known. He rewrote Eq. (40) on the implicit form

$$\frac{F_p}{\bar{v}\left(x_i + \frac{l_p}{\delta_i^*}(f_i) \cdot \delta_i^*(x_i)\right) - v_p(p_p)} = f_i \quad (42)$$

with

$$f_i(x_i, p_p) = \frac{p_p/p_i - 1}{\frac{1}{2}\gamma M_i^2 C_{f_i} F_p} \quad (43)$$

and

$$\frac{l_p}{\delta_i^*} = f\left(F_p / (\bar{v}_p - v_p)\right) \quad (44)$$

which is found from the interaction length law, see Figure 21. Equation 42 is solved iteratively for x_i .

The generalized free interaction theory has shown good agreement with nozzle test data in the interaction region. Figure 22 shows a comparison between calculated and measured pressure distribution in the Volvo S7 short nozzle, performed by Östlund.

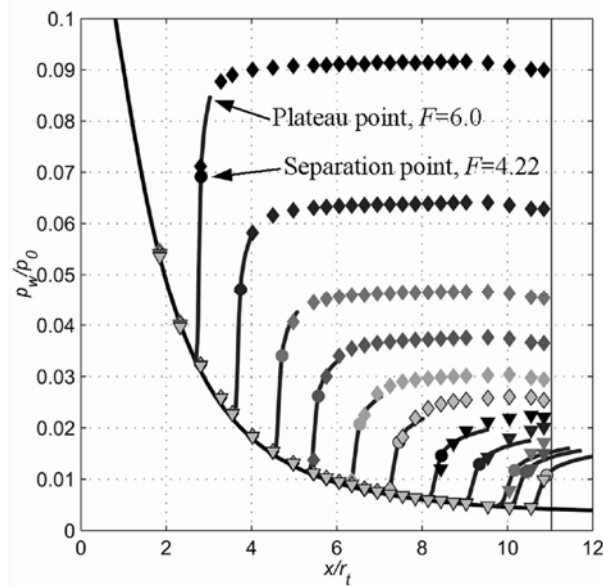


Figure 22: Predicted and measured wall pressure profile in the Volvo S7 short nozzle, from [1]

6 Semi-empirical models based on the generalized free interaction theory

The corner stones in the semi-empirical models by Reijasse & Birkemeyer [22] and Zerjeski [8] are the generalized free interaction theory developed by Carrière and momentum calculation over the recirculation region. Zerjeski's model is based on the model by Reijasse & Birkemeyer, with some changes in the calculation of the recirculation region. The two models are described more in detail below.

6.1 Model by Reijasse & Birkemeyer

The basic principle of the model is momentum conservation over the separated flow, i.e. the recirculation region. Figure 23 shows a “detailed” illustration of the flow field and pressure distribution in the recirculation region. The boundaries of the recirculation region are the nozzle wall, the upper limit of the mixing layer and a cross-section at the nozzle exit between the mixing layer and the nozzle wall. To be able to compute the momentum, it is necessarily to have information about the pressure and velocity profile on the boundaries.

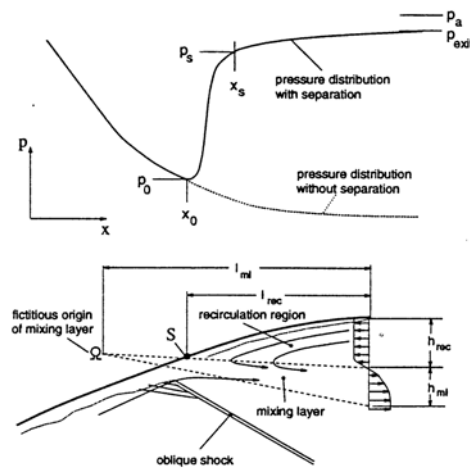


Figure 23: Flow field and pressure distribution, from R&B [22]

As mentioned earlier, an oblique shock is formed when the boundary layer separates from the nozzle wall. Downstream the shock, are the jet and the ambient medium mixed together in a mixing layer. Consider Figure 23 and it can be realized that the upper limit of the mixing layer is the lower (inner) limit of the recirculation region. In this model is the calculation of the flow field (and pressure distribution) subdivided into three major parts; the conical shock, the mixing layer and the boundary layer upstream the separation point.

6.1.1 Flow field

The conical shock: The direction of the flow field upstream the separation point is given by the nozzle contour. At the separation point a mixing layer starts to be formed. The direction of the mixing layer is said to be directly connected to the deflection over the shock. Reijasse & Birkemeyer uses the well know oblique shock relations (section 4.4) to determine the shock- and the deflection angle. The oblique shock equations (Eqs. 27-31) have five equations with six unknowns. Reijasse & Birkemeyer solves this by using the generalized free interaction theory (section 5.3.2) to calculate the pressure rise over the shock (p/p_0), and thus are they able to solve the oblique shock relations.

Mixing layer: The calculation of the mixing layer is made with the relations for an isobaric, incompressible, turbulent mixing layer, given by Görtler [23]. These relations can be used for a compressible and rotational flow with some modifications described in [24] and [25] respectively. The method by Görtler is only made for mixing layers with zero initial boundary layer thickness and therefore is a fictitious origin upstream the separation point integrated in the model, see Figure 23. The fictitious origin is determined from the boundary layer thickness at the separation point, which is originated from the boundary layer upstream the separation point.

Boundary layer: Both the calculation of the mixing layer and the generalized free interaction theory needs the properties of the boundary layer upstream the separation point. Reijasse & Birkemeyer estimates the boundary layer at the wall with the relations for a flat plate given by Michael [26].

6.1.2 Momentum calculations

To be able to compute the momentum on the recirculation region, the pressure distribution far downstream the interaction point must be determined. As seen in Figure 23, the missing part of the pressure distribution can be estimated with a linear distribution. The restrictions on the estimated pressure distributions can be seen in Figure 24; the minimum exit pressure is equal to the pressure calculated with generalized free interaction theory and the maximum exit pressure is equal the ambient pressure.

In the calculation of the momentum on the mixing layer boundary, the pressure is assumed to be constant in the vertical direction (in the recirculation region). It therefore remains to compute the momentum at the nozzle exit. Through LDV (Laser Doppler Velocitymetry) experiments and numerical simulations, Reijasse & Birkemeyer made the assumptions that the in flow velocity profile and the pressure at the nozzle exit are constant. Since the velocity at the inner boundary (at the mixing layer) is zero, a reduction factor of 0.9 of the height of the recirculation region at the nozzle exit is introduced for compensation.

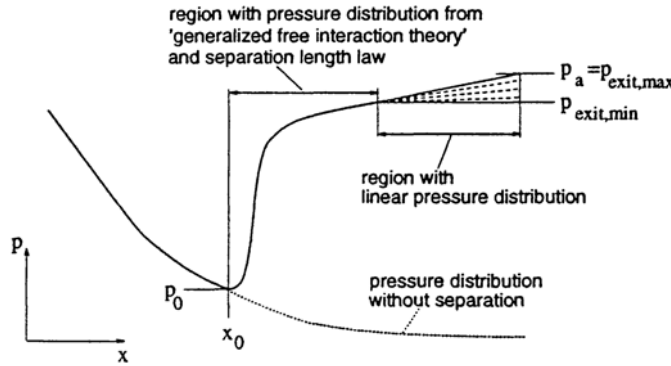


Figure 24: Linear pressure distribution downstream of the interaction region, R&B [22]

6.1.3 Determination of the separation point

The determination of the separation point for a given pressure ratio is done by iteration, starting with a virtual separation point near the nozzle throat. There the interaction length law and the generalized free interaction theory are applied to calculate the pressure distribution in the recirculation region (completed, if necessary with a linear pressure distribution). If the conservation of the momentum is satisfied, the virtual separation point is the real one. A variety of solutions can be found and therefore is the procedure repeated for other virtual separation points downstream the throat. The final solution is the mean value of the solutions.

6.1.4 Results of Reijasse & Birkemeyer model

Reijasse & Birkemeyer verified the model by comparing calculations with experimental values on two nozzles, a TIC and a LEA nozzle; the results are presented in Figure 25.

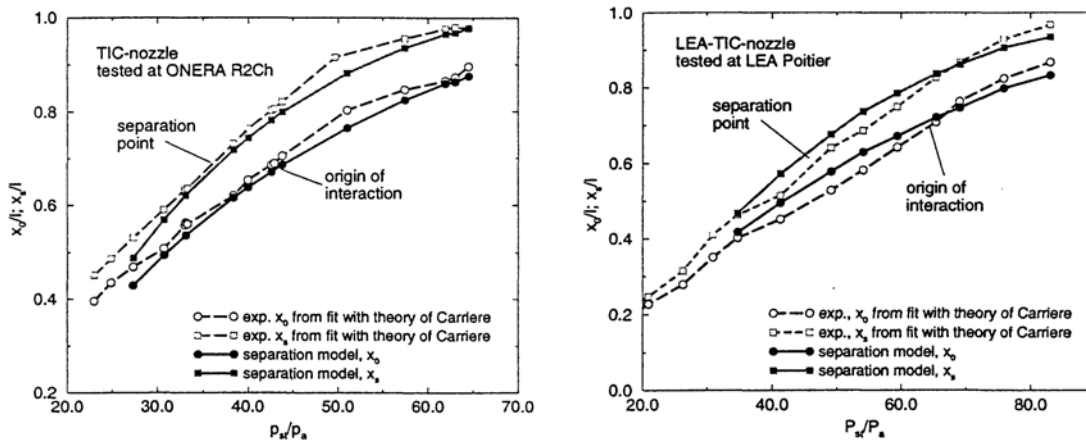


Figure 25: Prediction of separation location in TIC and LEA nozzle, R&B [22]

The prediction of the separation point shows good agreement with the experimental values for both nozzles. The maximum difference between the predicted and the experimental separation point is less than 5% of the nozzle length.

6.2 Model by Zerjeski

The model by Zerjeski is an extended version of Reijasse & Birkemeyer's model. The generalized free interaction theory and momentum calculations are still the basic principle of the model. The computation of the model together with the changes compared to Reijasse & Birkemeyer's model is described below. The characteristics of the flow are illustrated in Figure 26.

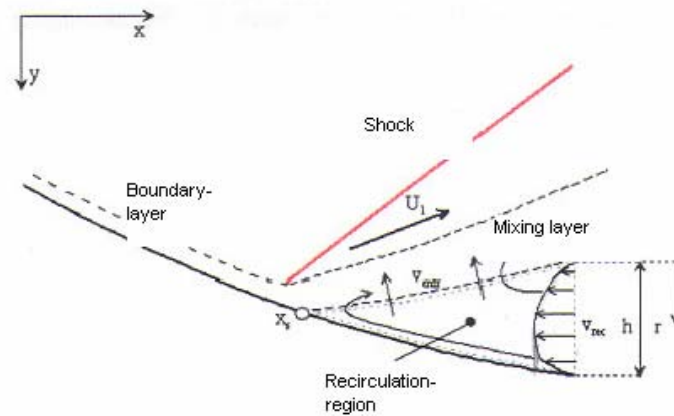


Figure 26: Characteristics of the flow, from Zerjeski [8].

6.2.1 Local flow parameters and boundary layer

The local flow parameters (M , T , ρ , and p) are determined by the area Mach number relation and the isotropic relation in section 2.1.1.

Zerjeski has extended the model by using boundary layer equations (upstream the incipient point) which are valid for hot gases and alternating wall temperature. The equations are derived by Reshotko & Tucker [27] from an Integration method for determination of turbulent boundary layers with a small pressure gradient. Comparison of the derived boundary layer thickness, displacement thickness and momentum thickness with TDK simulations showed good agreement. But the comparison of the friction coefficient C_f showed poor agreement. The model by Michel (used in Reijasse & Birkemeyer model) for a flat plate showed good agreement for the friction coefficient and is therefore used in the model.

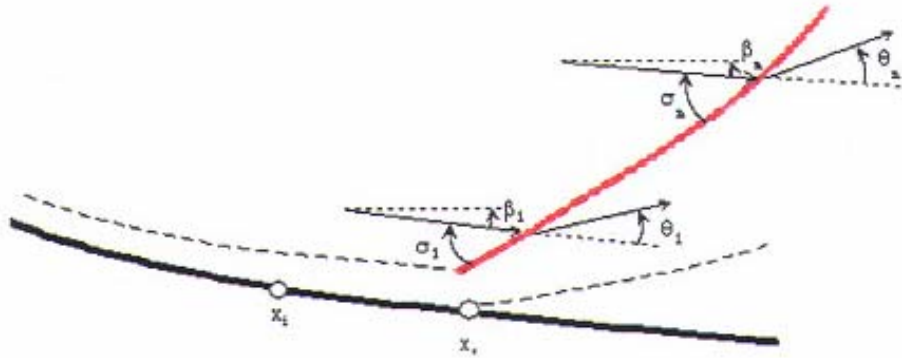


Figure 26: Determination of the shock, from Zerjeski [8]

6.2.2 Shock and mixing layer growth

The derivation of the shock is done by an iteration process of the oblique shock relations downstream the nozzle, illustrated in Figure 26. The pressure is assumed constant behind the shock and is determined from the generalized free interaction theory. At every new point of the shock are the local flow parameters calculated and used in the oblique shock relations.

The method which Zerjeski uses to compute the mixing layer is based on the theory by Görtler, used in Reijasse & Birkemeyer's model. Papamoschou & Roshko [28] followed up the work by Görtler, and defined some equations for the mixing layer growth for incompressible gases. Transformation of the mixing layer growth to compressible and axisymmetrical flow is made by the ratios by Brummund & Scheel [29] and Schlichting [30] respectively. This approach also has the advantage that no fictitious origin is needed, since the opening angle of the mixing layer can be found from a tangent function of the mixing layer growth.

The direction of the mixing layer is also slightly changed compared with the model by Reijasse & Birkemeyer. In Reijasse & Birkemeyer's model the direction is said to be equal to the deflection angle over the shock. But the mixing layer is slightly pushed into the ambient low velocity gas in the recirculation region, and thereby deflects the mixing layer direction. Schlichting [30] defined the deflection to 0.7° .

The last thing to determine is the velocity profile in the recirculation region before the momentum calculations can be performed. Brown and Roshko found a relation between the deflected jet velocity U_1 and the inflow velocity v_{ent} at the outer boundary of the mixing layer. To determine the velocity profile v_{rec} , Zerjeski approximated the velocity profile by a 6 grade function. With a calculation of the mass balance in the recirculation region, $v_{rec,max}$ can be determined and thus the velocity profile. The pressure p_{rec} is determined through isotropic relations.

6.2.3 Momentum calculation and prediction of separation point

Same procedure as in Reijasse & Birkemeyer's model is used to calculate the momentum on the recirculation region, see Figure 28. Momentum conservation calculations are made for both the x and y direction.

Zerjeski's iteration process to predict the separation point is illustrated in Appendix 1 (in German). Due to some losses in the model is the momentum conservation (Impulshalterung) not fulfilled, with the consequence that the interruption criterion does not work.

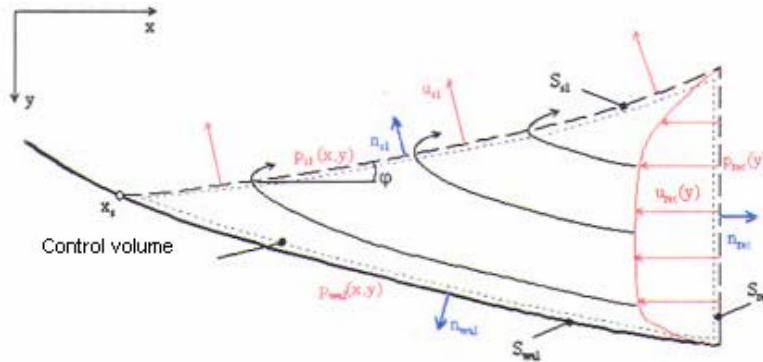


Figure 28: Properties at the recirculation region boundaries, [8]

6.2.4 Results of Zerjeski model

Zerjeski validated the model on a subscale TIC nozzle operated with cold gas. By fitting the model with one experiment, the losses mentioned above were found and thus could the model be used. The model showed good agreement for the four different pressure ratios (p_t/p_a), 35, 40, 45 and 50. The predicted separation points differed to the experimental value with, 5.5, 0.69, 1.0 and 0.42 % of the nozzle length respectively. The calculated pressure distributions showed good agreement, see Figure 29

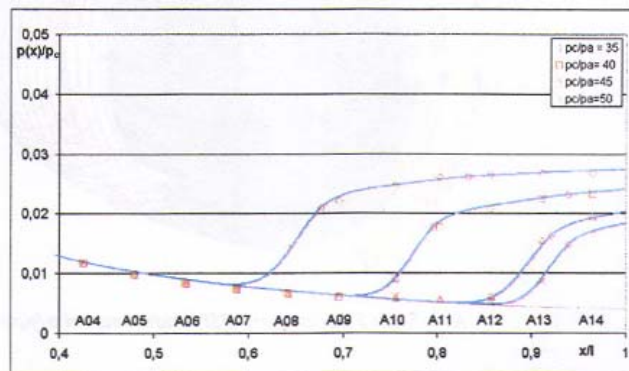


Figure 29: Calculated and experimental wall pressure distributions, [8]

6.3 Summary of the current models

The two models described above shows good agreement with performed experiments. But they have the weakness that they are only developed and tested for cold gases. The model by Zerjeski includes hot gases and alternating wall temperatures upstream the separation point, but not after the shock where the ambient- and jet gas mixes together. Another weakness in the models is a generalization of a constant (or constant increment of the) pressure distribution downstream the interaction region. What happens in the recirculation region therefore depends on the interaction region where the generalized free interaction theory is applied. Increasing the reliability in a new model demands two separately calculations; one in the interaction region and one in the recirculation region. That is applied in Malik and Tagirov's model, see Figure 20.

7 New model for the recirculation region

As a first step to build a more reliable model, various parameters of the jet and the ambient medium, and the mixing dynamic between the two gases inside the nozzle must be included. The model developed below, is a version of an integral method developed by Ginevsky [31] to calculate mixing layer thicknesses in turbulent mixing flows. The model takes the following parameters into account; jet and ambient gas adiabatic exponent (γ_i , γ_e), molecular weight of the jet and ambient gas (μ_i , μ_e), total temperature of the jet and ambient gas (T_{0i} , T_{0e}), and the nozzle wall contour in the separation zone ($r_w(x)$).

7.1 Model

To take gas compressibility (due to high velocity) and axial symmetry of the flow into account, the following two assumptions are made;

- profiles of the excess velocities and of the total enthalpy are self-similar with respect to the dimensionless variable obtained when converting from lateral coordinates y to new coordinate η with Dorodnitsyn-Mangler's transform;
- turbulent viscosity μ_t defined with the second Prandtl formula is constant across the viscous region and is equal to

$$\mu_t = \chi \rho_{0.5} |u_i - u_e| \Lambda, \quad (45)$$

where $\rho_{0.5}$ is density at the mixing layer line where $H_{0.5} = 0.5(H_e + H_i)$ and $u_{0.5} = 0.5(u_e + u_i)$, and Λ is a turbulence scale defined with the following equation:

$$\Lambda = (u_i - u_e) \left| \frac{\partial u}{\partial y} \right|_{\max} \quad (46)$$

The jet flow behind the nozzle is usually divided into three regions, the initially, transient and main section.

The main section lies at a substantial distance from the nozzle exit. The pressure across the jet flattens out and the jet flow becomes isobaric.

The transient section, where the jet flow is weakly nonisobaric, lies between the initial and main sections. The process of the viscous mixing is the governing process at the transient section. At that, influence of a nonisobaric pattern becomes negligible.

The flow at the initial section of a supersonic overexpanded jet is most interested from the viewpoint of solving the stated problem concerning the nozzle separation zone flow. The initial section stretches between the nozzle exit and where the inner mixing layer boundary reaches the jet axis

7.2 Isobaric jet

In the case, when the off-design pressure ratio doesn't significantly differ from unity, the rate of mixing layer growth is close to the one corresponding to outflow of an isobaric jet, i.e. a jet that is out-flowing into boundless space without any pressure gradient ($\nabla P=0$). The flow is called co-flow if the ambient medium flows in the same direction as the jet and counter-flow if it flows in the opposite direction. To compute the mixing layer growth, different techniques to manipulate the boundary-layer equations is used. The boundary-layer equations for compressible, axisymmetric turbulent flow can be written as [32];

Continuity:

$$\frac{\partial}{\partial x}(y\rho u) + \frac{\partial}{\partial y}(y\rho v) = 0 \quad (47)$$

Momentum:

$$\rho u y \frac{\partial u}{\partial x} + \rho v y \frac{\partial u}{\partial y} + y \frac{dP}{dx} = \frac{\partial}{\partial y} \left[y(\mu + \mu_t) \frac{\partial u}{\partial y} \right] \quad (48)$$

assume,

$$\frac{\partial \rho}{\partial t} = 0, \frac{\partial u}{\partial t} = 0 :$$

Let's introduce the velocity component in the mixing layer Δu (excess velocity) with the following equation:

$$\Delta u = \frac{u - u_e}{u_i - u_e} \quad (49)$$

Differentiate Eq. (51) with respect to x,

$$\frac{dP}{dx} = -\rho_e u_e \frac{du_e}{dx} (1 + \tan^2 \theta), \quad (52)$$

where θ is the angle of velocity vector inclination with respect to the x-axis. It is close to the nozzle wall angle.

Continuing by using the boundary-layer equation for compressible, axisymmetric turbulent flow (Eq. (47) and Eq. (48)). Use Eq. (47) and replace u by $u - u_e$ in Eq. (48), the momentum equation can then be transformed to the following form:

$$\frac{\partial}{\partial x} [\rho u y (u - u_e)] + \frac{\partial}{\partial y} [\rho v y (u - u_e)] + \left[\rho v y \frac{du_e}{dx} + y \frac{dP}{dx} \right] = \frac{\partial}{\partial y} \left[y (\mu + \mu_t) \frac{\partial (u - u_e)}{\partial y} \right] \quad (53)$$

Integrating this equation from y_i to y_w (nozzle wall radius), for simplicity Eq. (53) is divided into 5 parts;

$$\begin{aligned} B1 &= \int_{y_i}^{y_w} \frac{\partial}{\partial x} [\rho u y (u - u_e)] dy = \int_{y_i}^{y_e} \frac{\partial}{\partial x} [\rho u y (u - u_e)] dy + \int_{y_i}^{y_w} \frac{\partial}{\partial x} [\rho u y (u_e - u_e)] dy = \int_{y_i}^{y_e} \frac{\partial}{\partial x} [\rho u y (u - u_e)] dy = \\ &= \left[PI: \frac{d}{dx} \int_{a(x)}^{b(x)} f(x, y) dy = \int_{a(x)}^{b(x)} \frac{\partial}{\partial x} f(x, y) dy + f(x, b(x)) b'(x) - f(x, a(x)) a'(x) \right] = \\ &= \frac{d}{dx} \int_{y_i}^{y_e} [\rho u y (u - u_e)] dy - (\rho u y (u - u_e))_{y_e} \frac{dy_e}{dx} + (\rho u y)_i (u_i - u_e) \frac{dy_i}{dx} = \\ &= \frac{d}{dx} \int_{y_i}^{y_e} [\rho u y (u - u_e)] dy - 0 + (\rho u y)_i (u_i - u_e) \frac{dy_i}{dx} \end{aligned}$$

$$\begin{aligned} C1 &= \int_{y_i}^{y_w} \frac{\partial}{\partial y} [\rho v y (u - u_e)] dy = \int_{y_i}^{y_e} \frac{\partial}{\partial y} [\rho v y (u - u_e)] dy + \int_{y_e}^{y_w} \frac{\partial}{\partial y} [\rho v y (u_e - u_e)] dy = \int_{y_i}^{y_e} \frac{\partial}{\partial y} [\rho v y (u - u_e)] dy \\ &= \left[\frac{d}{dx} \int_{a(x)}^{b(x)} f(x, y) dy = \int_{a(x)}^{b(x)} \frac{\partial}{\partial x} f(x, y) dy + f(x, b(x)) b'(x) - f(x, a(x)) a'(x) \right] = \\ &= \left[I.B.P.: \int_a^b f(x) g(x) dx = [F(x) g(x)]_a^b - \int_a^b F(x) g'(x) dx \right] = [1 \rho v y (u - u_e)]_{y_i}^{y_e} - \int_{y_i}^{y_e} 0 \rho v y (u - u_e) dy \\ &= (\rho v y)_i (u_i - u_e) \end{aligned}$$

$$D1 = \int_{y_i}^{y_w} \rho v y \frac{du_e}{dx} dy = \int_{y_i}^{y_e} \rho v y \frac{du_e}{dx} dy + \int_{y_e}^{y_w} \rho v y \frac{du_e}{dx} dy = \frac{du_e}{dx} \int_{y_i}^{y_e} \rho v y dy + \frac{1}{2} (y_w^2 - y_e^2) u_e \rho_e \frac{du_e}{dx}$$

$$E1 = \int_{y_i}^{y_w} y \frac{dP}{dx} dy = \frac{1}{2} (y_w^2 - y_i^2) \frac{dP}{dx} = [eq(2)] = -\frac{1}{2} (y_w^2 - y_i^2) \rho_e u_e \frac{du_e}{dx} (1 + \tan^2 \theta)$$

$$\begin{aligned} F1 &= \int_{y_i}^{y_w} \frac{\partial}{\partial y} \left[y(\mu + \mu_t) \frac{\partial(u - u_e)}{\partial y} \right] dy = [I.B.P] = \\ &= \int_{y_i}^{y_e} \frac{\partial}{\partial y} \left[y(\mu + \mu_t) \frac{\partial(u - u_e)}{\partial y} \right] dy + \int_{y_e}^{y_w} \frac{\partial}{\partial y} \left[y(\mu + \mu_t) \frac{\partial(u_e - u_e)}{\partial y} \right] dy = [I.B.P] = \\ &= \left[y(\mu + \mu_t) \frac{\partial(u - u_e)}{\partial y} \right]_{y_i}^{y_e} - \int_{y_i}^{y_e} 0 \left[y(\mu + \mu_t) \frac{\partial(u - u_e)}{\partial y} \right] dy = y_i (\mu + \mu_t) \frac{\partial(u_i - u_e)}{\partial y} = 0 \end{aligned}$$

Use equations B1-F1 and rewrite Eq. (53):

$$\begin{aligned} &\frac{\partial}{\partial x} \int_{y_i}^{y_e} [\rho u y (u - u_e)] dy + (\rho u y)_i (u_i - u_e) \frac{dy_i}{dx} - (\rho v y)_i (u_i - u_e) + \frac{du_e}{dx} \int_{y_i}^{y_e} \rho u y dy \\ &+ \frac{1}{2} (y_w^2 - y_e^2) u_e \rho_e \frac{du_e}{dx} - \frac{1}{2} (y_w^2 - y_i^2) \rho_e u_e \frac{du_e}{dx} (1 + \tan^2 \theta) = 0 \end{aligned} \quad (54)$$

Divide Eq. (54) on both sides with $u_i - u_e$:

$$\begin{aligned} &\frac{1}{u_i - u_e} \frac{\partial}{\partial x} \int_{y_i}^{y_e} [\rho u y (u - u_e)] dy + (\rho u y)_i \frac{dy_i}{dx} - (\rho v y)_i + \frac{1}{u_i - u_e} \left[\frac{du_e}{dx} \int_{y_i}^{y_e} \rho u y dy + \right. \\ &\left. + \frac{1}{2} (y_w^2 - y_e^2) u_e \rho_e \frac{du_e}{dx} - \frac{1}{2} (y_w^2 - y_i^2) \rho_e u_e \frac{du_e}{dx} (1 + \tan^2 \theta) \right] = 0 \end{aligned} \quad (55)$$

The first term in Eq. (55) can be written as

$$\begin{aligned} &\frac{1}{u_i - u_e} \frac{\partial}{\partial x} \int_{y_i}^{y_e} [\rho u y (u - u_e)] dy = \frac{\partial}{\partial x} \int_{y_i}^{y_e} \rho u y \frac{(u - u_e)}{u_i - u_e} dy + \frac{d}{dx} \ln(u_i - u_e) \int_{y_i}^{y_e} \rho u y \frac{u - u_e}{u_i - u_e} dy = \\ &= \frac{\partial}{\partial x} \int_{y_i}^{y_e} \rho u y \Delta u dy + \frac{d}{dx} \ln(u_i - u_e) \int_{y_i}^{y_e} \rho u y \Delta u dy \end{aligned} \quad (56)$$

Combining Eq. (55) and Eq. (56), the momentum equation transforms to the following form:

$$\frac{\partial}{\partial x} \int_{y_i}^{y_e} \rho u y \Delta u dy + (\rho u y)_i \frac{dy_i}{dx} - (\rho v y)_i + A = 0 \quad (57)$$

where

$$A = \frac{d}{dx} \ln(u_i - u_e) \int_{y_i}^{y_e} \rho u y \Delta u dy + \frac{1}{u_i - u_e} \left[\frac{du_e}{dx} \int_{y_i}^{y_e} \rho u y dy + \frac{1}{2} (y_w^2 - y_e^2) u_e \rho_e \frac{du_e}{dx} - \frac{1}{2} (y_w^2 - y_i^2) \rho_e u_e \frac{du_e}{dx} (1 + \tan^2 \theta) \right] = 0 \quad (58)$$

Multiplying the momentum equation (Eq. (48)) with $2u$ and using the continuity equation (Eq (47)), it transforms the momentum equation to the following form:

$$\frac{\partial}{\partial x} [\rho u y (u^2 - u_e^2)] + \frac{\partial}{\partial y} [\rho v y (u^2 - u_e^2)] + \left[2\rho u y u_e \frac{du_e}{dx} + 2u y \frac{dP}{dx} \right] = 2u \frac{\partial}{\partial y} \left[y(\mu + \mu_t) \frac{\partial u}{\partial y} \right] \quad (59)$$

Integrating this equation from y_i to y_w , (for simplicity Eq. (59) is divided into 5 parts);

$$B2 = \frac{\partial}{\partial x} \int_{y_i}^{y_w} \rho u y (u^2 - u_e^2) dy = \frac{\partial}{\partial x} \int_{y_i}^{y_e} \rho u y (u^2 - u_e^2) dy + (\rho v y)_i \frac{dy_i}{dx} (u_i^2 - u_e^2) \quad (60b)$$

$$C2 = \int_{y_i}^{y_w} \frac{\partial}{\partial y} [\rho v y (u^2 - u_e^2)] dy = [I.B.P] = (\rho v y)_i (u_i^2 - u_e^2) \quad (60c)$$

$$D2 = \int_{y_i}^{y_w} 2\rho u y u_e \frac{du_e}{dx} dy = \int_{y_i}^{y_e} 2\rho u y u_e \frac{du_e}{dx} dy + \int_{y_e}^{y_w} 2\rho u y u_e \frac{du_e}{dx} dy = 2u_e \frac{du_e}{dx} \int_{y_i}^{y_e} \rho u y dy + 2\rho_e u_e^2 \frac{du_e}{dx} \frac{y_w^2 - y_e^2}{2} \quad (60d)$$

$$E2 = \int_{y_i}^{y_w} 2u y \frac{dP}{dx} dy = \int_{y_i}^{y_e} 2u y \frac{dP}{dx} dy + \int_{y_e}^{y_w} 2u y \frac{dP}{dx} dy = 2 \frac{dP}{dx} \int_{y_i}^{y_e} u y dy + \left[2u_e \frac{dP}{dx} \frac{y^2}{2} \right]_{y_e}^{y_w} = [Eq.(52)] = -2\rho_e u_e \frac{du_e}{dx} (1 + \tan^2 \theta) \int_{y_i}^{y_e} u y dy - \rho_e u_e^2 \frac{du_e}{dx} (1 + \tan^2 \theta) (y_w^2 - y_e^2) \quad (60e)$$

$$\begin{aligned}
F2 &= \int_{y_i}^{y_w} 2u \frac{\partial}{\partial y} \left[y(\mu + \mu_t) \frac{\partial u}{\partial y} \right] dy = \int_{y_i}^{y_e} 2u \frac{\partial}{\partial y} \left[y(\mu + \mu_t) \frac{\partial u}{\partial y} \right] dy = [I.B.P] = \\
&= 2 \left[uy(\mu + \mu_t) \frac{\partial u}{\partial y} \right]_{y_i}^{y_e} - 2 \int_{y_i}^{y_e} y(\mu + \mu_t) \frac{\partial u}{\partial y} \frac{\partial u}{\partial y} dy = \left[\frac{\partial u_i}{\partial y} = 0, \frac{\partial u_e}{\partial y} = 0 \right] = \quad (60f) \\
&= -2 \int_{y_i}^{y_e} y(\mu + \mu_t) \left(\frac{\partial u}{\partial y} \right)^2 dy
\end{aligned}$$

Divide Eqs. (60 b-f) with $u_i^2 - u_e^2$ and use the same technique as in Eq. (56), and also:

$$\frac{u^2 - u_e^2}{u_i^2 - u_e^2} = \frac{u - u_e}{u_i - u_e} \frac{u + u_e}{u_i + u_e} = [Eq(49)] = \Delta u \frac{u + u_e}{u_i + u_e} \quad (61a)$$

$$\frac{\partial \Delta u}{\partial y} = \frac{\partial}{\partial y} \left(\frac{u - u_e}{u_i - u_e} \right) \leftrightarrow \frac{\partial u}{\partial y} = (u_i - u_e) \frac{\partial \Delta u}{\partial y} \quad (61b)$$

Finally we obtain:

$$\begin{aligned}
&\frac{\partial}{\partial x} \int_{y_i}^{y_e} \rho u y \Delta u \frac{u + u_e}{u_i + u_e} dy + \frac{d}{dx} \ln(u_i^2 - u_e^2) \int_{y_i}^{y_e} \rho u y \frac{u^2 - u_e^2}{u_i^2 - u_e^2} dy + (\rho v y)_i \frac{dy_i}{dx} - (\rho v y)_i + \\
&+ \frac{1}{u_i^2 - u_e^2} \left[2u_e \frac{du_e}{dx} \int_{y_i}^{y_e} \rho u y dy + 2\rho_e u_e^2 \frac{du_e}{dx} \frac{y_w^2 - y_e^2}{2} - 2\rho_e u_e \frac{du_e}{dx} (1 + \tan^2 \theta) \int_{y_i}^{y_e} u y dy - \right. \\
&\left. - \rho_e u_e^2 \frac{du_e}{dx} (1 + \tan^2 \theta) (y_w^2 - y_e^2) \right] = -\frac{2}{u_i^2 - u_e^2} \int_{y_i}^{y_e} y(\mu + \mu_t) \left(\frac{\partial u}{\partial y} \right)^2 dy = \quad (62) \\
&= -\frac{2}{u_i^2 - u_e^2} \int_{y_i}^{y_e} y(\mu + \mu_t) \left(\frac{\partial \Delta u}{\partial y} (u_i - u_e) \right)^2 dy = -\frac{2(u_i - u_e)}{u_i + u_e} \int_{y_i}^{y_e} y(\mu + \mu_t) \left(\frac{\partial \Delta u}{\partial y} \right)^2 dy
\end{aligned}$$

simplified,

$$\frac{\partial}{\partial x} \int_{y_i}^{y_e} \rho u y \Delta u \frac{u + u_e}{u_i + u_e} dy + (\rho v y)_i \frac{dy_i}{dx} - (\rho v y)_i + B = -\frac{2(u_i - u_e)}{u_i + u_e} \int_{y_i}^{y_e} y(\mu + \mu_t) \left(\frac{\partial \Delta u}{\partial y} \right)^2 dy \quad (63)$$

where

$$B = \frac{d}{dx} \ln(u_i^2 - u_e^2) \int_{y_i}^{y_e} \rho u y \frac{u^2 - u_e^2}{u_i^2 - u_e^2} dy + \frac{1}{u_i^2 - u_e^2} \left[2u_e \frac{du_e}{dx} \int_{y_i}^{y_e} \rho u y dy - \right. \\ \left. - 2\rho_e u_e \frac{du_e}{dx} (1 + \tan^2 \theta) \int_{y_i}^{y_e} u y dy - \rho_e u_e^2 \frac{du_e}{dx} (y_w^2 - y_e^2) \tan^2 \theta \right] \quad (64)$$

Subtracting Eq. (63) from Eq. (57)

$$\frac{\partial}{\partial x} \int_{y_i}^{y_e} \rho u y \Delta u dy - \frac{\partial}{\partial x} \int_{y_i}^{y_e} \rho u y \Delta u \frac{u + u_e}{u_i + u_e} dy + (A - B) = \frac{\partial}{\partial x} \int_{y_i}^{y_e} \rho u y \Delta u \left(1 - \frac{u + u_e}{u_i + u_e} \right) dy + (A - B) = \\ = \frac{\partial}{\partial x} \int_{y_i}^{y_e} \rho u y \Delta u \left(1 - \frac{u + u_e}{u_i + u_e} \right) dy + (A - B) = \frac{2(u_i - u_e)}{u_i + u_e} \int_{y_i}^{y_e} y (\mu + \mu_t) \left(\frac{\partial \Delta u}{\partial y} \right)^2 dy = \quad (65) \\ = [\mu = \nu \rho] = \frac{2(u_i - u_e)}{u_i + u_e} \int_{y_i}^{y_e} \rho y (\nu + \nu_t) \left(\frac{\partial \Delta u}{\partial y} \right)^2 dy$$

Hereinafter we will only consider turbulent flows, i.e. $\nu_t \gg \nu$. To describe turbulent flows, we use the second Prantl formula providing good result for mixing layers:

$$\nu_t = \chi(u_i - u_e) \Lambda \quad (66)$$

Here χ is an empirical constant, Λ is a turbulence scale defined with the following formula:

$$\Lambda = (u_i - u_e) / |\partial u / \partial y|_{\max} = [Eq.(49)] = 1 / |\partial \Delta u / \partial y|_{\max}, \quad (67)$$

where $|\partial \Delta u / \partial y|_{\max}$ denotes the maximum absolute value of the indicated derivative.

Eq. (65) describes a compressible mixing layer flow. In contrast to the case of incompressible mixing layer flows, there are not so many experimental data which can be used for determination of the constant χ and function Δu form. In the case of incompressible flow, experimental data show that mixing layer velocity profiles are similar:

$$\Delta u = f(\eta^*),$$

where $\eta^* = (y - y_i) / \delta_D$, δ_D is the mixing layer thickness.

Let's transform the coordinates in accordance to Dorodnitsyn-Mangler's transform which allow us to convert compressible and axisymetrical flow boundary layer equations into equations that are similar to incompressible planar flow boundary layer equations:

$$\rho_a^0 r_a^0 \delta_D d\eta = \rho y dy \quad (68)$$

where ρ_a^0, r_a^0 are the density and radius of the ideal jet, δ_D is the mixing layer thickness in the transformed coordinates. The relations for y and η are determined from the following relations:

$$\eta = \frac{1}{\rho_a^0 r_a^0 \delta_D} \int_{y_i}^y \rho y dy \quad (69)$$

$$y^2 = y_i^2 + 2r_a^0 \delta_D \int_0^\eta \frac{\rho_a^0}{\rho} d\eta$$

Assume that similarity of mixing layer velocity profiles is valid for compressible flows too. But this similarity is not valid in the physical coordinates y , but in Dorodnitsyn-Mangler's coordinates η .

Therefore, we can write:

$$\Delta u = f(\eta) \quad (70)$$

If to assume that the Prantl number* (Pr) and Schmitt number** (Sc) are equal to 1, the following similarity equations across the mixing layer are valid:

$$\Delta H = (H - H_e)/(H_i - H_e) = c = \Delta u = f(\eta), \quad (71)$$

where H is the total enthalpy of the flow and c is the concentration of the jet gas in the mixing layer.

Let's introduce two relations that are used to simplify the following calculations:

$$u_e^* = \frac{u_e}{u_i - u_e} \quad (72)$$

$$u_e^{**} = \frac{u_e}{u_i}$$

* Def. Prantl number $Pr = \frac{c_p \mu}{k}$, where k is the thermal conductivity, ($Pr=0.72$ for standard conditions) [33]

** Def. Schmitt number; The ratio of the turbulent diffusivity for momentum to the turbulent diffusivity describing the mass transfer process, [33]

Substituting Eqs. (66), (67) and (68) into equation (65), start with the right side:

$$\begin{aligned}
B3 &= \frac{2(u_i - u_e)}{u_i + u_e} \int_{y_i}^{y_e} \left[\rho y (v + v_i) \left(\frac{\partial \Delta u}{\partial y} \right)^2 \right] dy = \\
&= \frac{2(u_i - u_e)}{u_i + u_e} \int_0^1 \left[\rho_a^0 r_a^0 \delta_D \left| \frac{\chi(u_i - u_e)}{\partial \Delta u / \left(\frac{\rho_a^0 r_a^0 \delta_D}{\rho y} \partial \eta \right)} \right|_{\max} \left(\frac{\frac{\partial \Delta u}{\rho_a^0 r_a^0 \delta_D \partial \eta}}{\frac{\rho y}{\rho y} \partial \eta} \right)^2 \right] d\eta \quad (73a) \\
&= \frac{2\chi(u_i - u_e)^2}{u_i + u_e} \int_0^1 \left[\frac{1}{\left| \frac{\partial \Delta u}{\rho y \partial \eta} \right|_{\max}} \left(\frac{\rho y \partial \Delta u}{\partial \eta} \right)^2 \right] d\eta
\end{aligned}$$

Now multiply both sides in Eq. (65) with $\frac{u_i + u_e}{(u_i - u_e)^2}$, compute the left side (use the same technique as in Eq. (56)):

$$\begin{aligned}
C3 &= \frac{u_i + u_e}{(u_i - u_e)^2} \frac{\partial}{\partial x} \int_{y_i}^{y_e} \rho u y \Delta u \left(1 - \frac{u + u_e}{u_i + u_e} \right) dy = \frac{\partial}{\partial x} \int_{y_i}^{y_e} \frac{u_i + u_e}{(u_i - u_e)^2} \rho u y \Delta u \left(1 - \frac{u + u_e}{u_i + u_e} \right) dy + \\
&+ \frac{d}{dx} \ln \left(\frac{(u_i - u_e)^2}{u_i + u_e} \right) \int_{y_i}^{y_e} \frac{u_i + u_e}{(u_i - u_e)^2} \rho u y \Delta u \left(1 - \frac{u + u_e}{u_i + u_e} \right) dy = \\
&= \left[\frac{u_i + u_e}{(u_i - u_e)^2} u \left(1 - \frac{u + u_e}{u_i + u_e} \right) \Delta u = \frac{u}{u_i - u_e} \left(\frac{u_i + u_e}{u_i - u_e} - \frac{u + u_e}{u_i - u_e} \right) \Delta u = [eg(50)] \right. \\
&= \frac{u_e + (u_i - u_e) \Delta u}{u_i - u_e} \left(\frac{u_i - u_e}{u_i - u_e} - \frac{u - u_e}{u_i - u_e} \right) \Delta u = (u_e^* + \Delta u) (1 - \Delta u) \Delta u = \\
&= \frac{\partial}{\partial x} \int_{y_i}^{y_e} \rho y \Delta u (u_e^* + \Delta u) (1 - \Delta u) \Delta u dy + \frac{d}{dx} \ln \left(\frac{(u_i - u_e)^2}{u_i + u_e} \right) \int_{y_i}^{y_e} \rho y \Delta u (u_e^* + \Delta u) (1 - \Delta u) dy = \\
&= \frac{d}{dx} \left[\rho_a^0 r_a^0 \delta_D \int_0^1 \Delta u (u_e^* + \Delta u) (1 - \Delta u) \Delta u d\eta \right] + \frac{d}{dx} \ln \left(\frac{(u_i - u_e)^2}{u_i + u_e} \right) \rho_a^0 r_a^0 \delta_D \int_0^1 \Delta u (u_e^* + \Delta u) (1 - \Delta u) d\eta \quad (73b)
\end{aligned}$$

Consider the integral:

$$\begin{aligned} \int_0^1 \Delta u (u_e^* + \Delta u) (1 - \Delta u) \Delta u d\eta &= \int_0^1 (u_e^* \Delta u - u_e^* \Delta u^2 + \Delta u^2 - \Delta u^3) d\eta = \\ &= u_e^* (A1 - A2) + A2 - A3, \end{aligned} \quad (73c)$$

where,

$$A1 = \int_0^1 \Delta u d\eta; A2 = \int_0^1 \Delta u^2 d\eta; A3 = \int_0^1 \Delta u^3 d\eta;$$

After these transformations Equation (65) can be written as:

$$\begin{aligned} \frac{d}{dx} \left[\rho_a^0 r_a^0 \delta_D \int_0^1 \Delta u (u_e^* + \Delta u) (1 - \Delta u) \Delta u d\eta \right] + \frac{d}{dx} \ln \left(\frac{(u_i - u_e)^2}{u_i + u_e} \right) \rho_a^0 r_a^0 \delta_D * \\ * \int_0^1 \Delta u (u_e^* + \Delta u) (1 - \Delta u) d\eta + \frac{u_i + u_e}{(u_i - u_e)^2} (A + B) = \end{aligned} \quad (74)$$

$$= 2\chi \int_0^1 \left[\frac{1}{\left| \rho y \frac{\partial \Delta u}{\partial \eta} \right|_{\max}} \left(\frac{\rho y \partial \Delta u}{\partial \eta} \right)^2 \right] d\eta$$

The integral on the right side can be represented in the following form:

$$\int_0^1 \left[\left(\rho y \frac{\partial \Delta u}{\partial \eta} \right)^2 \right] d\eta \approx \overline{(\rho y)^2} \int_0^1 \left(\frac{\partial \Delta u}{\partial \eta} \right)^2 d\eta = \overline{(\rho y)^2} A4, \quad (75)$$

where $A4 = \int_0^1 \left(\frac{\partial \Delta u}{\partial \eta} \right)^2 d\eta$ and $\overline{(\rho y)^2}$ is an average value of $(\rho y)^2$ across the mixing

layer. The denominator $\left| \rho y \frac{\partial u}{\partial \eta} \right|_{\max}$ can also be rewritten to simplify the calculations:

$$\left| \rho y \frac{\partial \Delta u}{\partial \eta} \right|_{\max} \approx (\rho y) \Big|_{n_{\max}} \left| \frac{\partial \Delta u}{\partial \eta} \right|_{\max} \quad (76)$$

where η_{\max} is the value on η where $\frac{\partial u}{\partial \eta}$ has maximum.

Before continuing, we introduce two relations that are frequently used in the following equations:

$$\begin{aligned} \frac{du_e^*}{dx} &= \frac{d}{dx} \left(\frac{u_e}{u_i - u_e} \right) = \frac{\frac{d}{dx}(u_i - u_e) - u_e \left(\frac{du_i}{dx} - \frac{du_e}{dx} \right)}{(u_i - u_e)^2} \Leftrightarrow \\ \Leftrightarrow \frac{du_e}{dx} &= \frac{(u_i - u_e)^2}{u_i} \frac{du_e}{dx} + \frac{u_e}{u_i} \frac{du_i}{dx} = \frac{(u_i - u_e)^2}{u_i} \frac{du_e^*}{dx} + u_e^{**} \frac{du_i}{dx} \end{aligned} \quad (77a)$$

$$\frac{du_e^{**}}{dx} = \frac{d}{dx} \left(\frac{u_e}{u_i} \right) = \frac{u_i \frac{du_e}{dx} - u_e \frac{du_i}{dx}}{u_i^2} \Leftrightarrow \frac{du_e}{dx} = u_i \frac{du_e^{**}}{dx} + u_e^{**} \frac{du_i}{dx} \quad (77b)$$

The first term in Eq. (74) can be written as:

$$\begin{aligned} B4 &= \frac{d}{dx} \left[\rho_a^0 r_a^0 \delta_D (u_e^* (A1 - A2) + A2 - A3) \right] = \\ &= \frac{d}{dx} \left[\rho_a^0 r_a^0 \delta_D (u_e^* (A1 - A2) + A2 - A3) + \rho_a^0 r_a^0 \delta_D \frac{du_e^*}{dx} (A1 - A2) \right] \end{aligned} \quad (78a)$$

Rewrite the second term on the left side in Eq. (74)

$$\begin{aligned} C4 &= \frac{d}{dx} \ln \left(\frac{(u_i - u_e)^2}{u_i + u_e} \right) \rho_a^0 r_a^0 \delta_D * \int_0^1 \Delta u (u_e^* + \Delta u) (1 - \Delta u) d\eta = \\ &= \left\{ 2 \left[\frac{1}{u_i - u_e} \left(\frac{du_i}{dx} - \frac{du_e}{dx} \right) \right] - \frac{1}{u_i + u_e} \left[\frac{du_i}{dx} + \frac{du_e}{dx} \right] \right\} \underbrace{\rho_a^0 r_a^0 \delta_D (u_e^* (A1 - A2) + A2 - A3)}_I = \\ &= \left\{ 2 \left[\frac{1}{u_i - u_e} \left(\frac{du_i}{dx} - \left(u_i \frac{du_e^{**}}{dx} + u_e^* \frac{du_i}{dx} \right) \right) \right] - \frac{1}{u_i + u_e} \left[\frac{du_i}{dx} + \left(u_i \frac{du_e^{**}}{dx} + u_e^* \frac{du_i}{dx} \right) \right] \right\} * I = \\ &= \frac{u_i}{u_i} \left\{ 2 \left[\frac{1}{u_i - u_e} \left(\frac{du_i}{dx} - \left(u_i \frac{du_e^{**}}{dx} + u_e^* \frac{du_i}{dx} \right) \right) \right] - \frac{1}{u_i + u_e} \left[\frac{du_i}{dx} + \left(u_i \frac{du_e^{**}}{dx} + u_e^* \frac{du_i}{dx} \right) \right] \right\} * I = \\ &= \left\{ 2 \left[\frac{1}{1 - u_e^{**}} \left(\frac{1}{u_i} \frac{du_i}{dx} - \left(\frac{du_e^{**}}{dx} + \frac{u_e^{**}}{u_i} \frac{du_i}{dx} \right) \right) \right] - \frac{1}{u_i + u_e} \left[\frac{1}{u_i} \frac{du_i}{dx} + \left(\frac{du_e^{**}}{dx} + \frac{u_e^{**}}{u_i} \frac{du_i}{dx} \right) \right] \right\} * I = \\ &= \left\{ 2 \left[\frac{1}{1 - u_e^{**}} \left(\frac{1}{u_i} \frac{du_i}{dx} - \left(\frac{du_e^{**}}{dx} + \frac{u_e^{**}}{u_i} \frac{du_i}{dx} \right) \right) \right] - \frac{1}{1 + u_e^{**}} \left[\frac{1}{u_i} \frac{du_i}{dx} + \left(\frac{du_e^{**}}{dx} + \frac{u_e^{**}}{u_i} \frac{du_i}{dx} \right) \right] \right\} * I = \end{aligned}$$

$$\begin{aligned}
&= \left\{ \frac{d}{dx} \ln u_i \left[\frac{2(1-u_e^{**})}{(1-u_e^{**})} - \frac{1+u_e^{**}}{1+u_e^{**}} \right] + \frac{du_e^{**}}{dx} \left[\frac{-2}{(1-u_e^{**})} - \frac{1}{1+u_e^{**}} \right] \right\} * I = \\
&= \left\{ \frac{d}{dx} \ln u_i - \frac{du_e^{**}}{dx} \left(\frac{3+u_e^{**}}{(1-u_e^{**})^2} \right) \right\} * \rho_a^0 r_a^0 \delta_D (u_e^* (A1 - A2) + A2 - A3)
\end{aligned} \tag{78b}$$

Continuing with terms from A and B, start with the terms without integrals:

$$\begin{aligned}
D4 &= \frac{u_i + u_e}{(u_i - u_e)^2} \left\{ \frac{1}{u_i - u_e} \left[\frac{1}{2} (y_w^2 - y_e^2) u_e \rho_e \frac{du_e}{dx} + \frac{1}{2} (y_w^2 - y_i^2) \rho_e u_e \frac{du_e}{dx} (1 + \tan^2 \theta) \right] - \right. \\
&\quad \left. - \frac{1}{u_i^2 - u_e^2} \left[\rho_e u_e^2 \frac{du_e}{dx} (y_w^2 - y_e^2) \tan^2 \theta \right] \right\} = \\
&= \left(\frac{u_i}{u_i} \right)^2 \frac{u_i + u_e}{(u_i - u_e)^2} \frac{u_e}{u_i - u_e} \rho_e \frac{du_e}{dx} \left\{ \left[\frac{1}{2} (y_w^2 - y_e^2) + \frac{1}{2} (y_w^2 - y_i^2) (1 + \tan^2 \theta) \right] - \right. \\
&\quad \left. - \frac{1}{u_i + u_e} [u_e (y_w^2 - y_e^2) \tan^2 \theta] \right\} = \left[\frac{u_e}{u_i + u_e} = \frac{u_i - u_e}{u_i + u_e} \frac{u_e}{u_i - u_e} = \frac{1 - u_e^{**}}{1 + u_e^{**}} u_e^* \right] = \\
&= \frac{1 + u_e^{**}}{(1 - u_e^{**})^2} u_e^* \rho_e \left(\frac{du_e^{**}}{dx} + u_e^{**} \frac{d}{dx} \ln u_i \right) * \\
&\quad * \left(\frac{1}{2} (y_w^2 - y_e^2) + \frac{1}{2} (y_w^2 - y_i^2) (1 + \tan^2 \theta) - \frac{1 - u_e^{**}}{1 + u_e^{**}} u_e^* [u_e (y_w^2 - y_e^2) \tan^2 \theta] \right)
\end{aligned} \tag{78c}$$

$$\begin{aligned}
E4 &= \frac{u_i + u_e}{(u_i - u_e)^2} \frac{d}{dx} \ln(u_i^2 - u_e^2) \int_{y_i}^{y_e} \rho u y \frac{u^2 - u_e^2}{u_i^2 - u_e^2} dy = \\
&= \frac{u_i + u_e}{(u_i - u_e)^2} \left[\frac{2}{u_i^2 - u_e^2} \left(u_i \frac{du_i}{dx} - u_e \frac{du_e}{dx} \right) \rho_a^0 r_a^0 \delta_D * \int_0^1 u \frac{u^2 - u_e^2}{u_i^2 - u_e^2} d\eta \right] = [eq(77b)] = \\
&= \rho_a^0 r_a^0 \delta_D \frac{u_i + u_e}{(u_i - u_e)^2} \left[\frac{2}{u_i^2 - u_e^2} \left(u_i \frac{du_i}{dx} - u_e \left(u_i \frac{du_e^{**}}{dx} + \frac{u_e}{u_i} \frac{du_i}{dx} \right) \right) \right] * \\
&\quad * \int_0^1 (u_e + (u_i - u_e) \Delta u) \frac{(u_e + (u_i - u_e) \Delta u)^2 - u_e^2}{u_i^2 - u_e^2} d\eta =
\end{aligned}$$

$$\begin{aligned}
&= \rho_a^0 r_a^0 \delta_D \frac{u_i + u_e}{(u_i - u_e)^2} \left[\frac{2}{(u_i^2 - u_e^2)^2} \left(\frac{du_i}{dx} \left(u_i - \frac{u_e^2}{u_i} \right) - u_e u_i \frac{du_e^{**}}{dx} \right) * \right. \\
&* \left. \int_0^1 \left(2u_e^2 (u_i - u_e) \Delta u + 3u_e ((u_i - u_e) \Delta u)^2 + ((u_i - u_e) \Delta u)^3 \right) d\eta \right] = \\
&= 2\rho_a^0 r_a^0 \delta_D \left[\left(\frac{du_i}{dx} - \frac{u_e u_i}{u_i^2 - u_e^2} \frac{du_e^{**}}{dx} \right) * \int_0^1 \left(2(u_e^*)^2 \Delta u + 3u_e^* (\Delta u)^2 + (\Delta u)^3 \right) d\eta \right] = \\
&= 2\rho_a^0 r_a^0 \delta_D \left[\left(\frac{du_i}{dx} - \frac{u_e^{**}}{1 - u_e^{**}} \frac{du_e^{**}}{dx} \right) * \left(2(u_e^*)^2 A1 + 3u_e^* A2 + A3 \right) \right]
\end{aligned} \tag{78d}$$

$$\begin{aligned}
F4 &= \frac{u_i + u_e}{(u_i - u_e)^2} \left[\frac{1}{u_i^2 - u_e^2} 2u_e \frac{du_e}{dx} \int_{y_i}^{y_e} \rho u y dy \right] = \\
&= \underbrace{\rho_a^0 r_a^0 \delta_D}_{I_3} \frac{1 + u_e^{**}}{1 - u_e^{**}} \left[\frac{2u_e}{(u_i^2 - u_e^2)(u_i - u_e)} \frac{du_e}{dx} \int_0^1 (u_e + (u_i - u_e) \Delta u) d\eta \right] = \\
&= I_3 \left\{ \frac{2}{(u_i + u_e)(u_i - u_e)} \left[u_i \frac{du_e^{**}}{dx} + u_e d \ln u_i \right] \int_0^1 \frac{(u_e + (u_i - u_e) \Delta u)}{(u_i - u_e)} d\eta \right\} = \\
&= \rho_a^0 r_a^0 \delta_D \frac{1 + u_e^{**}}{1 - u_e^{**}} \left\{ \frac{2u_e^*}{(1 + u_e^{**})} \left[u_i \frac{du_e^{**}}{dx} + u_e^{**} d \ln u_i \right] (u_e^* + A1) \right\}
\end{aligned} \tag{78e}$$

$$\begin{aligned}
G4 &= \frac{u_i + u_e}{(u_i - u_e)^2} \frac{1}{u_i^2 - u_e^2} \left[-2\rho_e u_e \frac{du_e}{dx} (1 + \tan^2 \theta) \int_{y_i}^{y_e} u y dy \right] = \left[\frac{\rho}{\rho} \right] = \\
&= -\frac{u_i + u_e}{(u_i - u_e)^2} \frac{1}{u_i^2 - u_e^2} \left[2\rho_e u_e \frac{du_e}{dx} (1 + \tan^2 \theta) \rho_a^0 r_a^0 \delta_D \int_0^1 \frac{u}{\rho} d\eta \right] = \\
&= -\rho_a^0 r_a^0 \delta_D \frac{u_i + u_e}{(u_i - u_e) u_i + u_e} \left\{ 2\rho_e \frac{u_e}{u_i - u_e} \left(u_i \frac{du_e^{**}}{dx} + u_e^{**} \frac{du_i}{dx} \right) (1 + \tan^2 \theta) \int_0^1 \frac{(u_e + (u_i - u_e) \Delta u)}{\rho (u_i - u_e)} d\eta \right\} = \\
&= -\rho_a^0 r_a^0 \delta_D \frac{1 + u_e^{**}}{1 - u_e^{**}} \left\{ \frac{2u_e^*}{1 + u_e^{**}} \left(\frac{du_e^{**}}{dx} + u_e^{**} \frac{d}{dx} \ln u_i \right) (1 + \tan^2 \theta) \rho_e \left[\int_0^1 \frac{u_e^*}{\rho} d\eta + \int_0^1 \frac{\Delta u}{\rho} d\eta \right] \right\}
\end{aligned} \tag{78f}$$

$$\begin{aligned}
H4 &= \frac{u_i + u_e}{(u_i - u_e)^2} \left\{ \frac{d}{dx} \ln(u_i - u_e) \int_{y_i}^{y_{ee}} \rho u y \Delta u dy \right\} = \\
&= \underbrace{\frac{1 + u_e^{**}}{1 - u_e^{**}} \rho_a^0 r_a^0 \delta_D}_{I_4} \left\{ \left[\frac{1}{u_i - u_e} \left(\frac{du_i}{dx} - \frac{du_e}{dx} \right) \right] \frac{1}{u_i - u_e} \int_0^1 (u_e + (u_i - u_e) \Delta u) \Delta u d\eta \right\} = \\
&= I_4 \left\{ \left[\frac{1}{u_i - u_e} \left(\frac{du_i}{dx} - \left(u_i \frac{du_e^{**}}{dx} + \frac{u_e}{u_i} \frac{du_i}{dx} \right) \right) \right] * \int_0^1 \frac{(u_e + (u_i - u_e) \Delta u) \Delta u}{u_i - u_e} d\eta \right\} = \quad (78g) \\
&= I_4 \left\{ \left[\frac{1}{u_i - u_e} \left(\frac{du_i}{dx} \left(1 - \frac{u_e}{u_i} \right) - u_i \frac{du_e^{**}}{dx} \right) \right] * [u_e^* A1 + A2] \right\} = \\
&= \frac{1 + u_e^{**}}{1 - u_e^{**}} \rho_a^0 r_a^0 \delta_D \left\{ \left[\frac{d}{dx} \ln u_i - \frac{1}{1 - u_e^{**}} \frac{du_e^{**}}{dx} \right] * [u_e^* A1 + A2] \right\}
\end{aligned}$$

$$\begin{aligned}
I4 &= \frac{u_i + u_e}{(u_i - u_e)^2} \left\{ \frac{1}{u_i - u_e} \frac{du_e}{dx} \int_{y_i}^{y_e} \rho u y dy \right\} = \\
&= \rho_a^0 r_a^0 \delta_D \frac{1 + u_e^{**}}{1 - u_e^{**}} \left\{ \frac{1}{u_i - u_e} \left(u_i \frac{du_e^{**}}{dx} + \frac{u_e}{u_i} \frac{du_i}{dx} \right) \int_0^1 \frac{(u_e + (u_i - u_e) \Delta u)}{u_i - u_e} d\eta \right\} = \quad (78h) \\
&= \rho_a^0 r_a^0 \delta_D \frac{1 + u_e^{**}}{1 - u_e^{**}} \left\{ \frac{1}{1 - u_e^{**}} \left(\frac{du_e^{**}}{dx} + u_e^{**} \frac{d}{dx} \ln u_i \right) (u_e^* + A1) \right\} = \\
&= \rho_a^0 r_a^0 \delta_D \frac{1 + u_e^{**}}{1 - u_e^{**}} \left\{ \frac{u_e^* + A1}{1 - u_e^{**}} \left(\frac{du_e^{**}}{dx} + u_e^{**} \frac{d}{dx} \ln u_i \right) \right\}
\end{aligned}$$

Finally, by combining equations (78a)-(78h) we will come up with a differential equation which describes the mixing layer growth:

$$\frac{d}{dx} (\rho_a^0 r_a^0 \delta_D) + \frac{\rho_a^0 r_a^0 \delta_D E}{u_e^* (A1 - A2) + A2 - A3} = \frac{D + C}{u_e^* (A1 - A2) + A2 - A3} \quad (79)$$

Where:

$$D = \frac{2 \overline{\chi(\rho y)^2} A4}{(\rho y) \Big|_{n_{\max}} \left| \frac{\partial \Delta u}{\partial \eta} \right|_{\max}}$$

$$\begin{aligned}
C &= \frac{1+u_e^{**}}{(1-u_e^{**})^2} u_e^* \rho_e \left(\frac{du_e^{**}}{dx} + u_e^{**} \frac{d}{dx} \ln u_i \right) * \\
&* \left(\frac{y_w^2 - y_e^2}{2} + \frac{y_w^2 - y_i^2}{2} (1 + \tan^2 \theta) - \frac{1-u_e^{**}}{1+u_e^{**}} u_e^* [u_e (y_w^2 - y_e^2) \tan^2 \theta] \right), \\
E &= \frac{du_e^*}{dx} (A1 - A2) + (u_e^* (A1 - A2) + A2 - A3) \left\{ \frac{d}{dx} \ln u_i - \frac{du_e^{**}}{dx} \left(\frac{3+u_e^{**}}{(1-u_e^{**})^2} \right) \right\} + \\
&+ \frac{1+u_e^{**}}{1-u_e^{**}} \left\{ [u_e^* A1 + A2] \left[\frac{1}{u_i - u_e} \left(\frac{du_i}{dx} \left(1 - \frac{u_e}{u_i} \right) - u_i \frac{du_e^{**}}{dx} \right) \right] \right\} + \left\{ \frac{u_e^* + A1}{1-u_e^{**}} \left(\frac{du_e^{**}}{dx} + u_e^{**} \frac{d}{dx} \ln u_i \right) \right\} - \\
&- 2 \frac{1-u_e^{**}}{1+u_e^{**}} \left[\left(\frac{du_i}{dx} - \frac{u_e^{**}}{1-u_e^{**}} \frac{du_e^{**}}{dx} \right) * (2(u_e^*)^2 A1 + 3u_e^* A2 + A3) \right] - \left\{ \frac{2u_e^*}{(1+u_e^{**})} (u_e^* + A1) * \right. \\
&* \left. \left[u_i \frac{du_e^{**}}{dx} + u_e^{**} d \ln u_i \right] \right\} + \left\{ \frac{2u_e^*}{1+u_e^{**}} \left(\frac{du_e^{**}}{dx} + u_e^{**} \frac{d}{dx} \ln u_i \right) (1 + \tan^2 \theta) \rho_e \left[\int_0^1 \frac{u_e^*}{\rho} d\eta + \int_0^1 \frac{\Delta u}{\rho} d\eta \right] \right\}
\end{aligned}$$

$$A1 = \int_0^1 \Delta u d\eta; A2 = \int_0^1 \Delta u^2 d\eta; A3 = \int_0^1 \Delta u^3 d\eta; A4 = \int_0^1 \left(\frac{\partial \Delta u}{\partial \eta} \right)^2 d\eta$$

Since the mixing layer thickness δ_D is defined in the transformed coordinates, we need a relation that can be used to describe the inner and outer boundary of the mixing layer in the physical coordinates.

The jet gas continuity equation can be written in the following form:

$$\int_0^{y_e} \rho u y c dy = \frac{1}{2} \rho_a u_a r_a^2 = const. \quad (80)$$

Here ρ_a , u_a and r_a are density, velocity and radius of the jet at the initial section. Rewrite the integral to the following form:

$$\int_0^{y_e} \rho u y c dy = \int_0^{y_i} \rho u y c dy + \int_{y_i}^{y_e} \rho u y c dy = \frac{1}{2} \rho_a^0 u_a^0 y_i^2 + \rho_a^0 r_a^0 \delta_D \int_0^1 u c d\eta = \frac{1}{2} \rho_a u_a r_a^2 \quad (81)$$

From this equation can we determine the location of the lower mixing layer boundary:

$$y_i^2 = \frac{\rho_a u_a}{\rho_a^0 u_a^0} r_a^2 - 2 \frac{r_a^0 \delta_D}{u_a^0} \int_0^1 u c d\eta. \quad (82a)$$

Using Eq. (50) to calculate the integral on the right side:

$$\begin{aligned} \int_0^1 u c d\eta &= \int_0^1 (u_e + (u_i - u_e)\Delta u) c d\eta = \int_0^1 (u_i - u_e) \left(\frac{u_e c}{u_i - u_e} + \Delta u c \right) d\eta = \\ &= (u_i - u_e) \int_0^1 (u_e^* c + \Delta u c) d\eta = [Eq.(71)] = (u_i - u_e)(u_e^* A1 + A2) \end{aligned} \quad (82b)$$

Therefore, the inner mixing layer boundary is determined by:

$$\begin{aligned} y_i^2 &= \frac{\rho_a u_a}{\rho_a^0 u_a^0} r_a^2 - 2r_a^0 \delta_D \frac{u_i - u_e}{u_a^0} (u_e^* A1 + A2) = \\ &= \frac{\rho_a u_a}{\rho_a^0 u_a^0} r_a^2 - 2r_a^0 \delta_D \frac{u_i}{u_a^0} (1 - u_e^{**}) (u_e^* A1 + A2) \end{aligned} \quad (82c)$$

The outer mixing layer boundary is determined from relation (69) (for $y=y_e$; $n=1$):

$$y_e^2 = y_i^2 + 2r_a^0 \delta_D \int_0^1 \frac{\rho_a^0}{\rho} d\eta = \left[extend \frac{\rho_i}{\rho_i} \right] = y_i^2 + 2r_a^0 \delta_D \frac{\rho_a^0}{\rho_i} \int_0^1 \frac{\rho_i}{\rho} d\eta \quad (83)$$

It is also necessary to determine the y position y_{mean}^2 and y_{max}^2 (Eq. (79)). They are determined from relation (69)

$$y_{max}^2 = y_i^2 + 2r_a^0 \delta_D \frac{\rho_a^0}{\rho_i} \int_0^{n_{max}} \frac{\rho_i}{\rho} d\eta \quad (84)$$

$$y_{mean}^2 \approx y_{0.5}^2 = y_i^2 + 2r_a^0 \delta_D \frac{\rho_a^0}{\rho_i} \int_0^{0.5} \frac{\rho_i}{\rho} d\eta \quad (85)$$

To solve these equations it is necessary to determine the dependence of ρ_i/ρ on η . Assume that the jet and ambient gases are ideal and don't react chemically with one another.

As pressure across the mixing layer is constant, we can write:

$$\frac{\rho_i}{\rho} = \frac{RT}{R_i T_i} = [h = c_p T] = \frac{R}{c_p} \frac{c_{pi}}{R_i} \frac{h}{h_i}, \quad (86)$$

where T , h , R and c_{pi} are temperature, enthalpy, individual gas constant and specific heat at constant pressure for the mixing gases (the jet gas and the ambient gas in the mixing layer). The same parameters marked with a subscript i are the jet gas parameters.

Enthalpy and internal energy are additive parameters, therefore:

$$\begin{aligned}\frac{c_p}{c_{pi}} &= c + (1-c) \frac{c_{pe}}{c_{pi}}, \\ \frac{R}{R_i} &= c + (1-c) \frac{\mu_i}{\mu_e},\end{aligned}\tag{87a}$$

where μ_i , μ_e are molecular weights of the jet and ambient gases, respectively, c_{pe} is ambient gas specific heat at constant pressure. Using the ideal gas R-c_p relation $\left(c_p = \frac{\gamma R}{\gamma - 1}\right)$, we can determine c_{pe}/c_{pi} :

$$\frac{c_{pe}}{c_{pi}} = \frac{\gamma_e(\gamma_i - 1)R_e}{\gamma_i(\gamma_e - 1)R_i} = \frac{\gamma_e(\gamma_i - 1)\mu_i}{\gamma_i(\gamma_e - 1)\mu_e},\tag{87b}$$

Therefore, we can write the required ρ_i/ρ relation in the following form:

$$\frac{\rho_i}{\rho} = \frac{h}{h_i} \frac{c + (1-c) \frac{\mu_i}{\mu_e}}{c + (1-c) \frac{\gamma_e(\gamma_i - 1)\mu_i}{\gamma_i(\gamma_e - 1)\mu_e}}\tag{88}$$

Value of h/h_i is determined from the total enthalpy relation:

$$H = c_p T_0 = \frac{\gamma R}{(\gamma - 1)} T_0 = \frac{\gamma T_0 \mathfrak{R}}{(\gamma - 1) \mu} = h + \frac{u^2}{2},\tag{89a}$$

This equation can be rewritten to the following form:

$$h = H_i [i_0 + (1 - i_0) \Delta H] - 0.5u^2\tag{89b}$$

$$\text{where, } i_0 = \frac{H_e}{H_i} = \frac{\frac{\mathfrak{R} \gamma_e T_{0e}}{\mu_e (\gamma_e - 1)}}{\frac{\mathfrak{R} \gamma_i T_{0i}}{\mu_i (\gamma_i - 1)}} = \frac{\gamma_e T_{0e} \mu_i (\gamma_i - 1)}{\gamma_i T_{0i} \mu_e (\gamma_e - 1)}.\tag{89c}$$

Substituting u from Eq. (50) and taking account of $\frac{u_i^2}{h_i} = (\gamma_i - 1)M_i^2$, we obtain:

$$\frac{h}{h_i} = \left(1 + \frac{\gamma_i - 1}{2} M_i^2\right) \left[i_0 + (1 - i_0) \Delta H \right] - \frac{\gamma_i - 1}{2} M_i^2 \left[u_e^{**} + (1 - u_e^{**}) \Delta u \right]^2 \quad (89d)$$

To determine a relation for the velocity at the outer boundary (u_e), we use the condition of zero mass flow rate of the ambient gas incoming from the atmosphere and ejected by the jet:

$$\begin{aligned} G_e &= \int_{y_i}^{y_w} \rho u (1 - c) y dy = \int_{y_i}^{y_e} \rho u (1 - c) y dy + \int_{y_e}^{y_w} \rho_e u_e y dy = \\ &= \rho_a^0 r_a^0 \delta_D \int_0^1 (u_e + (u_i - u_e) \Delta u) (1 - c) d\eta + \frac{1}{2} \rho_e u_e (y_w^2 - y_e^2) = \\ &= \rho_a^0 r_a^0 \delta_D (u_i - u_e) \int_0^1 (u_e^* + \Delta u) (1 - c) d\eta + \frac{1}{2} \rho_e u_e (y_w^2 - y_e^2) = \\ &= \rho_a^0 r_a^0 \delta_D (u_i - u_e) \left\{ \left[u_e^* (1 - A1) + A1 - A2 \right] + \frac{\frac{1}{2} \rho_e u_e^* (y_w^2 - y_e^2)}{\rho_a^0 r_a^0 \delta_D} \right\} = 0 \Rightarrow \\ \Rightarrow u_e^* &= - \frac{A1 - A2}{1 - A1 + \frac{\rho_e (y_w^2 - y_e^2)}{2 \rho_a^0 r_a^0 \delta_D}} \end{aligned} \quad (90)$$

Note that this relation is valid at $y_w > y_e$. At $y_w = y_e$ Eq. (90) have a more simple form:

$$u_e^* = - \frac{A1 - A2}{1 - A1}, \quad (91)$$

i.e. $u_e^* = \text{const}$. It is necessary to note that this occurs even when $\delta_D \neq 0$.

When u_e^* is determined it is easy to find a relation for u_e^{**} :

$$u_e^* = \frac{u_e}{u_i - u_e} = \frac{u_e^{**}}{1 - u_e^{**}} \Leftrightarrow u_e^{**} = \frac{u_e^*}{1 + u_e^*} \quad (92)$$

Remains to determine the pressure distribution along the separated zone. In a first approximation, flow near the nozzle wall can be considered as low-velocity one, therefore, we can use Bernoulli's equation for determination of the pressure distribution:

$$\begin{aligned}
P_w + \frac{1}{2} \rho_e u_e^2 (1 + \tan^2 \theta_w) &= P_a \Rightarrow P_w \left[1 + \frac{1}{2 P_i} \rho_e u_e^2 (1 + \tan^2 \theta_w) \right] = P_a \Leftrightarrow \\
\Leftrightarrow P_w \left[1 + \frac{\gamma_i}{a_i^2 \rho_i} \frac{1}{2} \rho_e u_e^2 (1 + \tan^2 \theta_w) \right] &= P_a \Leftrightarrow P_w \left[1 + \frac{\gamma_i}{2} \frac{M_i^2}{u_i^2} \frac{\rho_e}{\rho_i} u_e^2 (1 + \tan^2 \theta_w) \right] = P_a \\
\Leftrightarrow P_w \left[1 + \frac{\gamma_i}{2} M_i^2 \frac{\rho_e}{\rho_i} (u_e^{**})^2 (1 + \tan^2 \theta_w) \right] &= P_a \Leftrightarrow \\
\Leftrightarrow \frac{P_w}{P_a} &= \frac{1}{1 + \frac{\gamma_i}{2} M_i^2 \frac{\rho_e}{\rho_i} (u_e^{**})^2 (1 + \tan^2 \theta_w)}, \tag{93}
\end{aligned}$$

Another method to determine the pressure distribution along the nozzle wall is to assume isentropic flow along the nozzle wall:

$$\frac{P_w}{P_a} = \left(1 + \frac{\gamma_e - 1}{2} M_e^2 \right)^{\frac{-\gamma_e}{\gamma_e - 1}}, \tag{94}$$

where M_e^2 is calculated with the following formula

$$\begin{aligned}
M_e^2 &= \frac{u_e^2}{a_e^2} (1 + \tan^2 \theta_w) = \frac{u_e^2}{u_i^2} M_i^2 \frac{a_i^2}{a_e^2} (1 + \tan^2 \theta_w) = (u_e^{**})^2 M_i^2 \frac{\rho_i}{\gamma_e P_e} (1 + \tan^2 \theta_w) = \\
&= \frac{\gamma_i}{\gamma_e} (u_e^{**})^2 M_i^2 \frac{\rho_e}{\rho_i} (1 + \tan^2 \theta_w)
\end{aligned}$$

Therefore,

$$\frac{P_w}{P_a} = \left(1 + \frac{\gamma_e - 1}{2} \frac{\gamma_i}{\gamma_e} (u_e^{**})^2 M_i^2 \frac{\rho_e}{\rho_i} (1 + \tan^2 \theta_w) \right)^{\frac{-\gamma_e}{\gamma_e - 1}} \tag{95}$$

As we have found the distribution P_w/P_a , we can determine P_s/P_e (P_2/P_3).

Summary of equation to be solved;

$$\frac{d}{dx}(\rho_a^0 r_a^0 \delta_D) + \frac{\rho_a^0 r_a^0 \delta_D E}{u_e^*(A1 - A2) + A2 - A3} = \frac{D + C}{u_e^*(A1 - A2) + A2 - A3} \quad (79)$$

$$y_i^2 = \frac{\rho_a u_a}{\rho_a^0 u_a^0} r_a^2 - 2r_a^0 \delta_D \frac{u_i}{u_a} (1 - u_e^{**}) (u_e^* A1 + A2) \quad (82c)$$

$$y_e^2 = y_i^2 + 2r_a^0 \delta_D \frac{\rho_a^0}{\rho_i} \int_0^1 \frac{\rho_i}{\rho} d\eta \quad (83)$$

$$y_{\max}^2 = y_i^2 + 2r_a^0 \delta_D \frac{\rho_a^0}{\rho_i} \int_0^{n_{\max}} \frac{\rho_i}{\rho} d\eta \quad (84)$$

$$y_{\text{mean}}^2 \approx y_{0.5}^2 = y_i^2 + 2r_a^0 \delta_D \frac{\rho_a^0}{\rho_i} \int_0^{0.5} \frac{\rho_i}{\rho} d\eta \quad (85)$$

$$u_e^* = -\frac{A1 - A2}{1 - A1 + \frac{\rho_e (y_w^2 - y_e^2)}{2\rho_a^0 r_a^0 \delta_D}} \quad (90)$$

$$\frac{P_w}{P_a} = \frac{1}{1 + \frac{\gamma_i}{2} M_i^2 \frac{\rho_e}{\rho_i} (u_e^{**})^2 (1 + \tan^2 \theta_w)} \quad (93)$$

or

$$\frac{P_w}{P_a} = \left(1 + \frac{\gamma_e - 1}{2} \frac{\gamma_i}{\gamma_e} (u_e^{**})^2 M_i^2 \frac{\rho_e}{\rho_i} (1 + \tan^2 \theta_w) \right)^{\frac{-\gamma_e}{\gamma_e - 1}} \quad (95)$$

7.3.2 Continuation Isobaric jet

For an isobaric jet in the initial section u_i and u_e are constants and $\nabla P=0$, which result in a more simple form of mixing layer growth equation (79):

$$\frac{d}{dx}(\rho_a^0 r_a^0 \delta_D) = \frac{D}{u_e^*(A1 - A2) + A2 - A3} \quad (96)$$

To determine the mixing layer growth in an isobaric flow Equation (96) and Equations (82b) and (83) are used. It should be noted that the mixing layer growth appears behind the nozzle since the nozzle is adapted.

7.3.3. Model for “gradientless” flow in the separated zone

The model for an isobaric jet can be used as a first approximation to calculate the mixing layer and the pressure distribution inside an overexpanded nozzle. Assume at first $\frac{dP}{dx} \approx u_e \rho_e \frac{du_e}{dx} \approx u_i \rho_i \frac{du_i}{dx} \approx 0$. At that, we can use the equations for an isobaric jet (section 7.3.2). There is although one exception compared to the isobaric jet model; the velocity component at the outer boundary of the mixing layer is not set to be constant and thus is the wall pressure distribution not constant. The velocity component and wall pressure are determined through Eq. (90) and Eq. (93) or Eq. (95) respectively. This approach is slightly contradictory, since, at first is the pressure gradient set to be zero and then it is calculated to differ from zero. The “gradientless” model is developed to be used as a comparison to the “real” model described in section 7.3.1.

8 Calculations

Before we can perform any calculations, we need to specify the velocity profile $\Delta u = f(\eta)$. There are three shapes that are mentioned in the literature [34].

- profile N1: $f(\eta) = 1 - 6\eta^2 + 8\eta^3 - 3\eta^4$. This profile is well suitable for description of flows of various types in mixing layers of axisymmetric, plane and co-flowing jets and wakes.
- profile N2: $f(\eta) = 1 - 3\eta^2 + 2\eta^3$. This profile is well suitable for approximation of mixing layer profile at the initial section of co-flowing jets.
- profile N3: $f(\eta) = (1 - \eta^{3/2})^2$ is well known Schlichting’s profile for velocity in plane turbulent wake far from the body.

The empirical constant χ in Eq. (66) is determined for each of the profiles by fitting it to experimental data [34].

Calculation of separation zone flows consist of two parts; a calculation of ideal gas jet shape and a calculation of mixing layer and separation zone flow parameters.

Determination of the geometric characteristics of the overexpanded ideal jet can be obtained with numerical methods allowing us to solve Euler’s equations. An addendum was included in the space marching Euler solver n2dsm (FORTRAN code developed at Volvo Aero). In ordinary cases is the nozzle wall radius $r_w(x)$ ($y_w(x)$) predefined, and the pressure distribution is computed. In the calculation of the ideal jet shape is the pressure distribution predefined and the ideal jet shape (y_w) is wanted. From the separation point

downstream the nozzle is the pressure prescribed by a stated pressure distribution ($P_{w,Goal}$). The target is to find an y_w which gives a pressure P_w equal to $P_{w,Goal}$. A solver for the stated problem is the Newton-Raphson method (97) [40]:

$$y_{w,i+1} = y_{w,i} - \frac{f(y_{w,i})}{f'(y_{w,i})} \quad (97)$$

where

$$f(y_w) = P_w(y_w) - P_{w,Goal} \quad (98)$$

and

$$f'(y_w) = \frac{P_w(y_w + \Delta y) - P_w(y_w - \Delta y)}{2\Delta y}. \quad (99)$$

with interruption criterion

$$\frac{|f|}{P_{w,Goal}} < 5 \cdot 10^{-4}. \quad (100)$$

At first is $y_{w,i}(x_n)$ approximated with $y_{w,i}(x_{n-1}) + \frac{dy_{w,i}(x_{n-1})}{dx} \Delta x$. At that point, are the pressures $P_w(y_{w,i})$, $P_w(y_{w,i}+\Delta y)$, and $P_w(y_{w,i}-\Delta y)$ calculated and $y_{w,i+1}$ is determined. The iteration continues until the interruption criterion is satisfied. The same procedure is repeated for every x downstream the nozzle ($x_n+\Delta x$).

The ideal jet characteristics ρ_a^0 and u_a^0 is determined through a flux averaging method [39]. The method is based on averaging the mass flux, momentum flux and energy flux through the surface ($0-y_w$) and finding the corresponding average flow states. The flow states are found from the Equations (101)

$$\begin{aligned} F_1 &= \rho_F u_F \\ F_2 &= \rho_F u_F^2 + p_F \\ F_3 &= \rho_F u_F v_F \\ F_4 &= \rho_F u_F H_F = \rho_F u_F \left(\frac{\gamma}{\gamma-1} \frac{p_F}{\rho_F} + \frac{1}{2} (u_F^2 + v_F^2) \right) \end{aligned} \quad (101)$$

Solving these equations gives

$$\begin{aligned}
p_F &= \frac{1}{\gamma-1} \left(F_2 \pm \sqrt{F_2^2 + (\gamma^2 - 1)(F_2^2 + F_3^2 - 2F_1F_4)} \right) \\
u_F &= \frac{F_2 - p_F}{F_1} \\
v_F &= \frac{F_3}{F_1} \\
\rho_F &= \frac{F_1}{u_F}
\end{aligned} \tag{102}$$

where $u_F = u_a^0$ and $\rho_F = \rho_a^0$. The \pm sign in p_F depends on the flow velocity, (+) subsonic- and (-) supersonic flow.

As an input to this program it is necessary to specify the following parameters:

γ_i – jet gas adiabatic exponent;

μ_i – molecular weight of the jet gas;

P_0 – total pressure (combustion pressure);

T_{0i} – total temperature of the jet gas;

M_i – Mach number at the nozzle just before the separation;

$n=p_i/p_a$ – jet off design pressure ratio (ratio of nozzle wall pressure to the ambient pressure) or ambient pressure;

In order to calculate the mixing layer and the separation zone flow, it is necessary to additionally specify the following parameters:

γ_e – ambient medium adiabatic exponent;

μ_e – molecular weight of the ambient medium gas;

T_{0e} – total temperature of the ambient medium gas;

$r_w(x)$ – nozzle wall contour in the separation zone.

The differential equation (Eq. (79) or (96)) is solved by Euler's method:

$$y_{n+1} = y_n + hf(x_n, y_n) \tag{103}$$

The integrals in Eq. (73c) are constants and differ depending on velocity profile $\Delta u = f(\eta)$.

8.1 Calculation methods

8.1.1 Calculation method 1

The derivatives $\frac{du_e^{**}}{dx}$ and $\frac{du_e^*}{dx}$ in Equation (79) (C and E) are unknowns. First are the

derivatives $\left(\frac{du_e^{**}}{dx}\right)_n$ and $\left(\frac{du_e^*}{dx}\right)_n$ estimated to be equal to the derivatives $\left(\frac{du_e^{**}}{dx}\right)_{n-1}$ and $\left(\frac{du_e^*}{dx}\right)_{n-1}$ respectively. Eq. (79), (82c), (83), (91) and (92) are then solved and the derivatives $\left(\frac{du_e^{**}}{dx}\right)_n$ and $\left(\frac{du_e^*}{dx}\right)_n$ are calculated. If the new derivatives differ from the old derivatives Eq. (79) is solved again (with the new ones). The iteration proceeds until the derivatives converge. The procedure is repeated for $x + \Delta x$ downstream the nozzle.

8.1.2 Calculation method 2

Another method was also tested to calculate the derivatives. Since the pressure is assumed to be equal on the inner and outer boundary of the mixing layer, the pressure gradient is equal. We can write the pressure gradient on the inner boundary:

$$\frac{dP}{dx} = -\rho_i u_i \frac{du_i}{dx} (1 + \tan^2 \theta_i) \quad (104)$$

Set Eq. (52) equal Eq. (104);

$$\begin{aligned} \rho_i u_i \frac{du_i}{dx} (1 + \tan^2 \theta_i) &= \rho_e u_e \frac{du_e}{dx} (1 + \tan^2 \theta) \Leftrightarrow \\ \Leftrightarrow \frac{du_i}{dx} (1 + \tan^2 \theta_i) &= \frac{\rho_e u_e}{\rho_i u_i} \frac{du_e}{dx} (1 + \tan^2 \theta) \Leftrightarrow \left[\text{Eq. (64b)}, \frac{\rho_e}{\rho_i} = \overline{\rho_e} \right] \\ \Leftrightarrow \frac{du_i}{dx} (1 + \tan^2 \theta_i) &= \frac{\overline{\rho_e} u_e}{u_i} \left(u_i \frac{du_e^{**}}{dx} + u_e^{**} \frac{du_i}{dx} \right) (1 + \tan^2 \theta) \Leftrightarrow \\ \Leftrightarrow \frac{1}{u_i} \frac{du_i}{dx} ((1 + \tan^2 \theta_i) - \overline{\rho_e} u_e^{**2} (1 + \tan^2 \theta)) &= \overline{\rho_e} u_e^{**} \frac{du_e^{**}}{dx} (1 + \tan^2 \theta) \Leftrightarrow \\ \Leftrightarrow \frac{du_e^{**}}{dx} &= \frac{\frac{1}{u_i} \frac{du_i}{dx} (1 + \tan^2 \theta_i) - \overline{\rho_e} u_e^{**2} (1 + \tan^2 \theta)}{\overline{\rho_e} u_e^{**} (1 + \tan^2 \theta)} \end{aligned} \quad (105)$$

Same technique is used to calculate $\frac{du_e^*}{dx}$,

$$\frac{du_e^*}{dx} = \frac{\frac{du_i}{dx} \left(\frac{(1 + \tan^2 \theta_i)}{(1 + \tan^2 \theta) \rho_e u_e^{**}} - u_e^{**} \right)}{(u_i - u_e)^2 u_i} \quad (106)$$

This method has the advantage that the iteration is only over Eq. (82c) and (83), which results in fewer calculations.

8.2 Validation

The validation of the model was subdivided into two parts; first was the isobaric jet model validated and then the calculation of the ideal jet shape.

8.2.1 Validation of the Isobaric jet model

The isobaric jet model was validated by examine the influence of the different parameters M_i , u_e^{**} , and i_0 on the initial length L_c . First was the influence of Mach number (M_i) examined. Reference [34] presents experimental data of various authors on the influence of Mach number M_i on the initial section length for isobaric jets. For the Mach range 0.3-2.5 the initial length can be approximated by the formula

$$L_c = 8.4 + 2.2M_i^2. \quad (107)$$

Calculation based on Eq. (96) and the experimental data (107) are presented in Figure 31. The calculations were performed with $\gamma_i = \gamma_e = 1.4$, $\mu_i = \mu_e = 29$, $i_0 = 1$ and $u_e^{**} = 0$. The constant χ in the turbulence viscosity formula (67) was determined to give a best fit for low velocities. It was determined to 0.00545, 0.0058, and 0.0062 for the velocity profiles N1, N2, and N3 respectively. One can see, as Mach number rises, the initial length rises too. The calculations qualitatively agree with the experimental curve showing the influence of compressibility, which validates the assumptions made in obtaining Equation (96). The comparison of the calculations with experimental data shows that the best agreement is attained when profile N1 is used. The N1 profile is therefore chosen to be used in all further calculations.

The next step was to validate the influence of u_e^{**} . If the ambient medium flows with velocity u_e^{**} in the same direction as the jet, the velocity difference $u_i - u_e$ decreases. That causes weakening of the mixing process and increases the initial section length. If the velocities of the ambient medium and the jet have the opposite directions, the difference $u_i - u_e$ increases, which intensifies the mixing process and decreases the initial length. Calculations performed at $u_e^{**} = 0.1$ and $u_e^{**} = -0.1$ together with experimental data [35] for

$u_e^{**}=0.1$ are presented in Figure 32. These calculations were performed with $\gamma_i = \gamma_e = 1.4$, $\mu_i = \mu_e = 29$, $i_0 = 1$. One can see that the calculation agrees well with the experimental data.

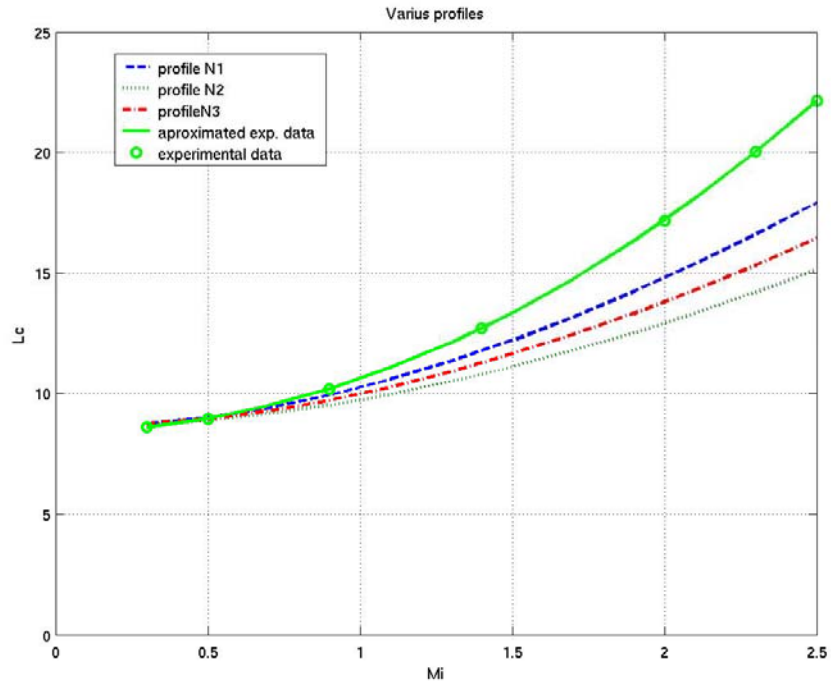


Figure 31: Initial length versus Mach number, for different velocity profiles

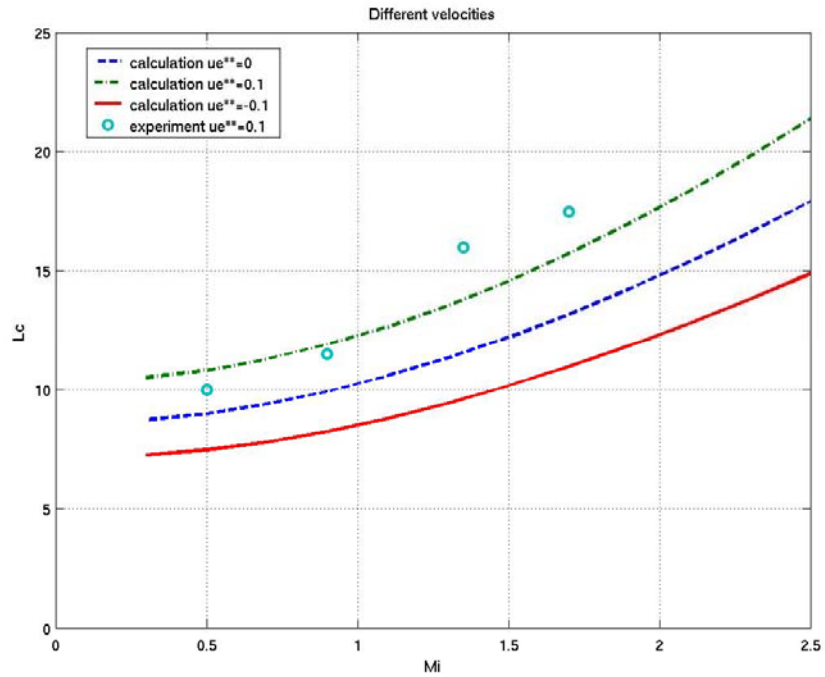


Figure 32: Initial length versus Mach number, for different velocity ratios

As the jet total temperature increases ($i_0 < 1$), the jet density becomes lower than the ambient medium density. That causes the jet to decay more rapidly and the initial length decreases. Vice versa happens as the total temperature decreases ($i_0 > 1$). Unfortunately no experimental data for various i_0 are available, but the calculations for $i_0=0.5$ and $i_0=2$, which are presented in Figure 33 shows the same trend as mentioned. These calculations were performed with $\gamma_i = \gamma_e = 1.4$, $\mu_i = \mu_e = 29$, $u_e^{**} = 0$.

The case with an ambient counter-flow is of most interest and is therefore examined further. A comparison of experimental data [36] with calculations is presented in Figure 34. One can see a good agreement of the calculation and the experimental data within the u_e^{**} range -0.4-0.

Performed calculations have shown qualitative and quantitative agreement of the obtained results with both the physical discourses and experimental data. Therefore, the obtained equations can be used for determination of the mixing layer characteristics for jets whose parameters differs from parameters of the ambient medium. At that, the jet gas flow compressibility governed by the Mach number M_i is taken into account properly.

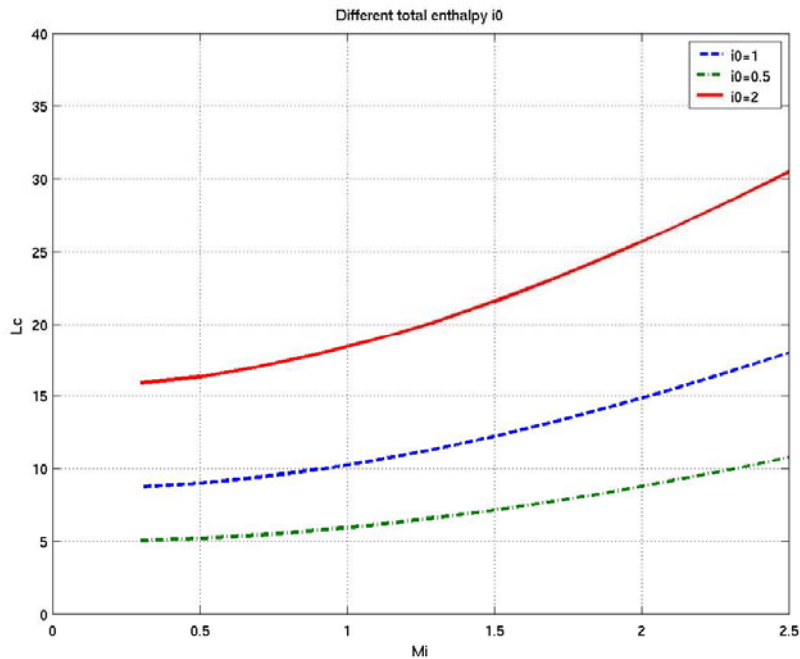


Figure 33: Influence of the total enthalpy on the initial length

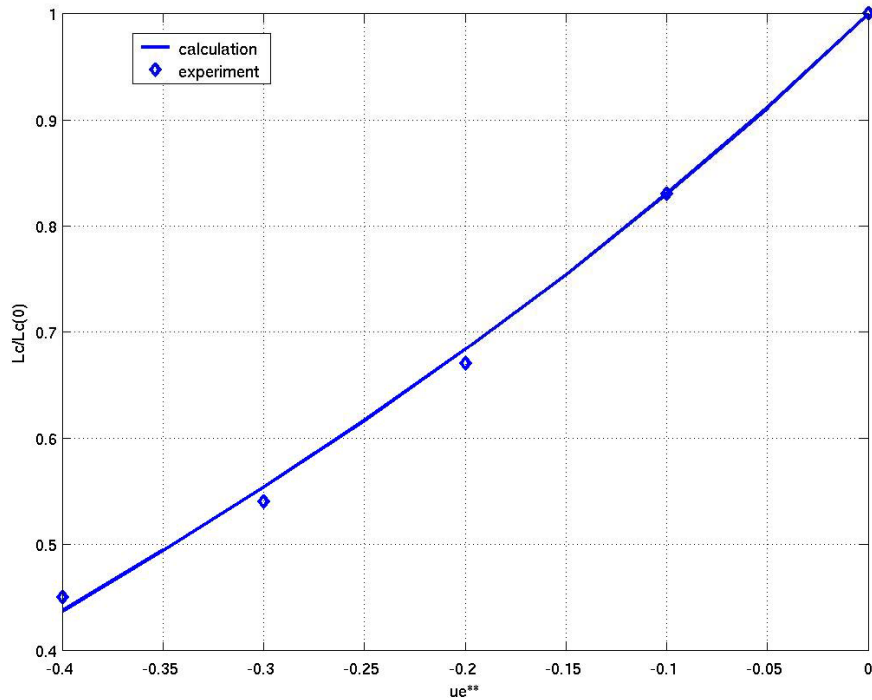


Figure 34: Influence of a counter-flow on the initial length

8.2.2 Validation of the geometric characteristics of an overexpanded ideal gas jet

Performed calculations with the program n2dsm were validated through data (tables) for conical flows [37]. Calculations were performed for various values on adiabatic exponent γ , Mach number M , conical nozzle wall angle θ , and off-design pressure ratio $n=P_w/P_a$. A comparison of the calculated ideal gas jet shapes with the tabled shapes for $\gamma=1.4$, $M=3$, $\theta=10^\circ$ are presented in Figure 35. The same comparison for $M=4$ and $M=5$ are presented in Figure 36. Influence of the nozzle wall angle θ is examined in Figure 37 at $\gamma=1.2$, $M=3$ and $n=0.4$. Figure 38 shows comparisons for different pressure ratios n at $\gamma=1.2$, $M=3$ and $\theta=10^\circ$. The influence on the adiabatic exponent γ can be examined by comparing Figure 35 with Figure 37 and Figure 36 with Figure 38. One can see from the figures that the calculated geometric characteristics have a good accuracy within wide range of Mach number, adiabatic exponent, nozzle wall angle, and off-design pressure ratio. The slightly difference between the published- and the calculated profiles can be explained by the different techniques that is used to calculate the velocity profile (before the shock). The profiles presented in [37] are from conical flows, i.e. a velocity profile which is constant over the whole cross section (y-dir). The program n2ds on the other hand computes the velocity profile in a conical nozzle. As can be seen in Figure 4, the velocity is not constant over the cross section and thus differs slightly from a conical flow.

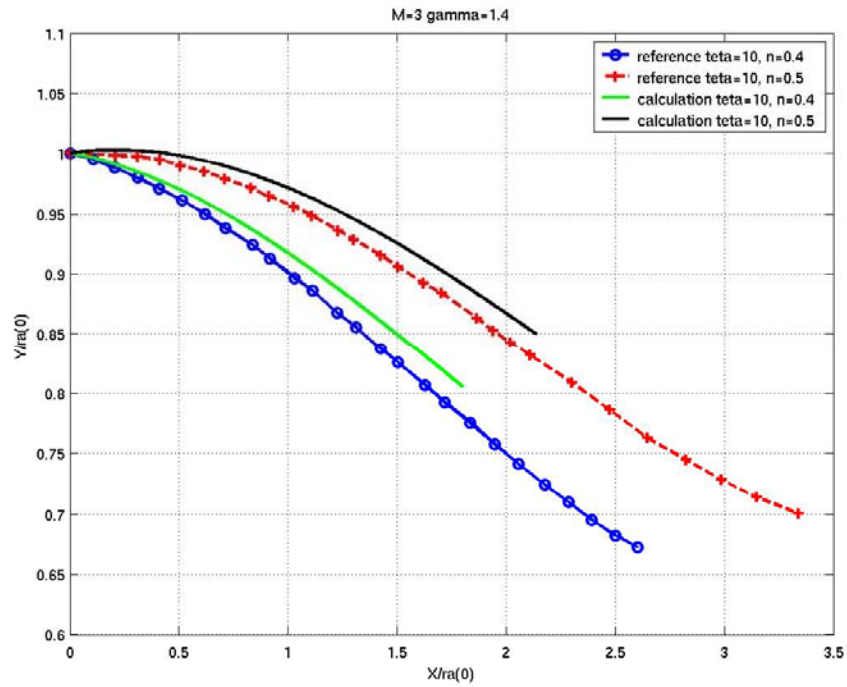


Figure 35: Comparison of calculated and published shapes of ideal gas jets for $M=3$; $\gamma=1.4$

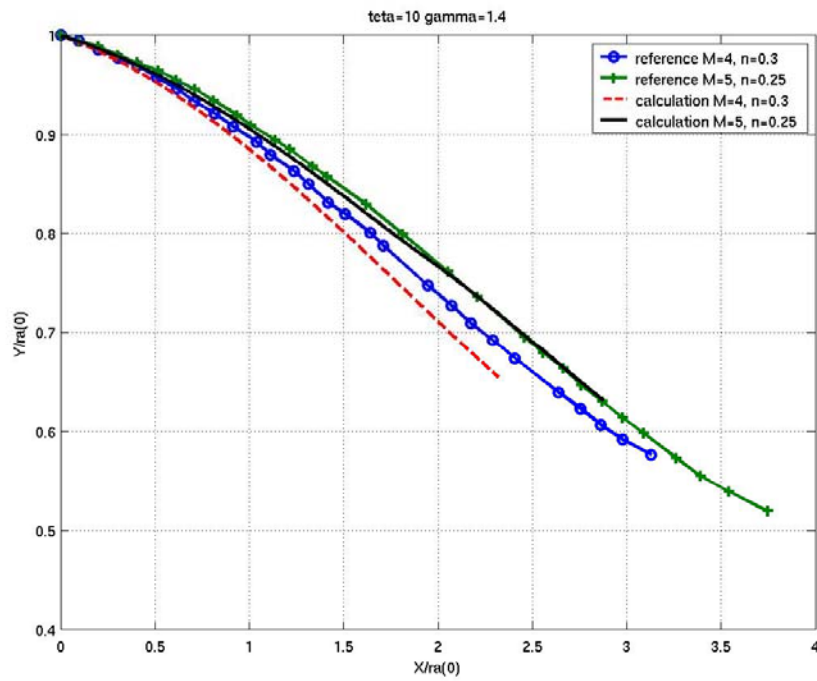


Figure 36: Comparison of calculated and published shapes for $M=4&5, \gamma=1.4$ and $\theta=10^\circ$

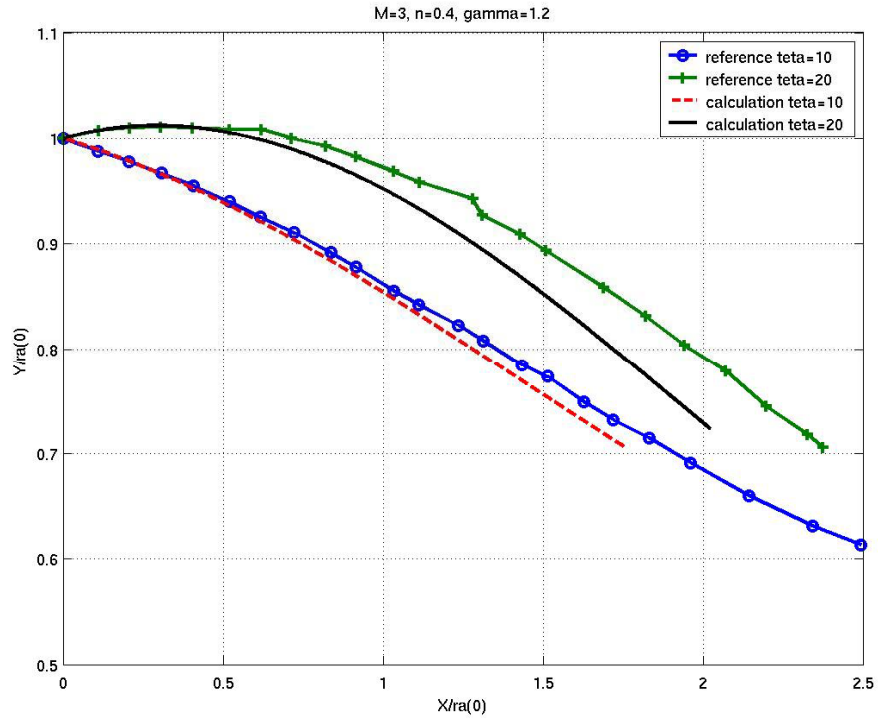


Figure 37: Comparison of calculated and published shapes for $M=3$, $\gamma=1.2$ and $n=0.4$

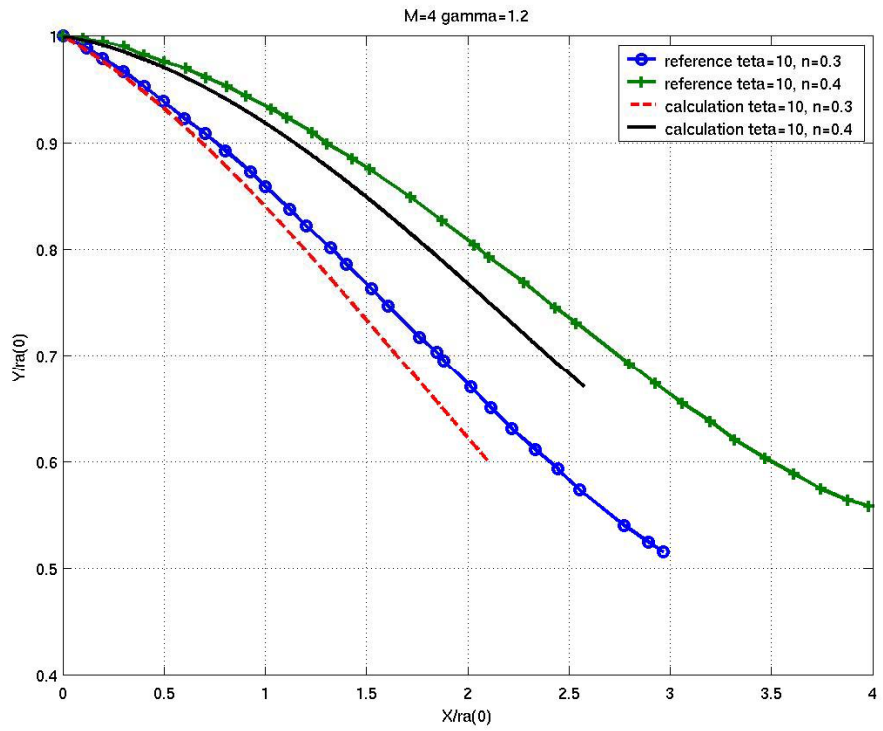


Figure 38: Comparison of calculated and published shapes for $M=4$, $\gamma=1.2$ and $\theta=10^\circ$

An additional test was also performed to validate the program n2dsm. The jet shape and the shock was computed and compared to a Schlieren photo [38], see Figure 39. The calculation and experiment was performed on the Volvo S6 nozzle, with air at $p_0=4.5$ MPa, $p_a=100$ kPa and $T_0=450$ K. The pressure distribution in n2dsm was set to the experimental pressure distribution [38]. Figure 38 shows good agreement between calculation and photo, which further strengthens the accuracy in n2dsm. Figure 40 illustrates the calculated Mach number distribution. It should be noted that n2dsm do not take a formation of a Mach disc into account, and thus continues to compute the shock until it reaches the symmetry axis. In this case was the iteration interrupted before it reached the symmetry axis.

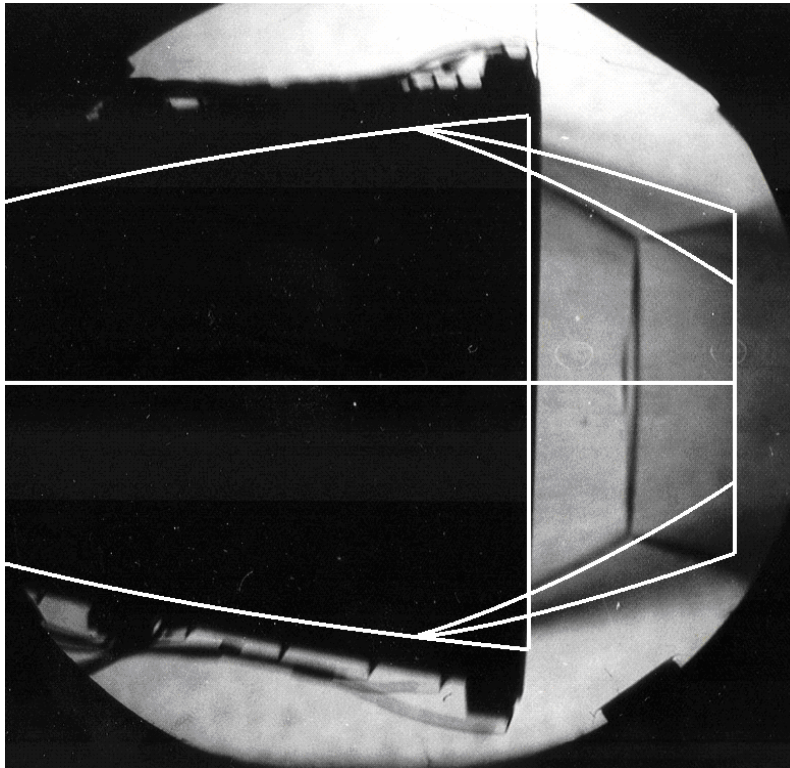


Figure 39: Calculation and Schlieren photo, overexpanded S6 nozzle at $p_0=4.5$ MPa.

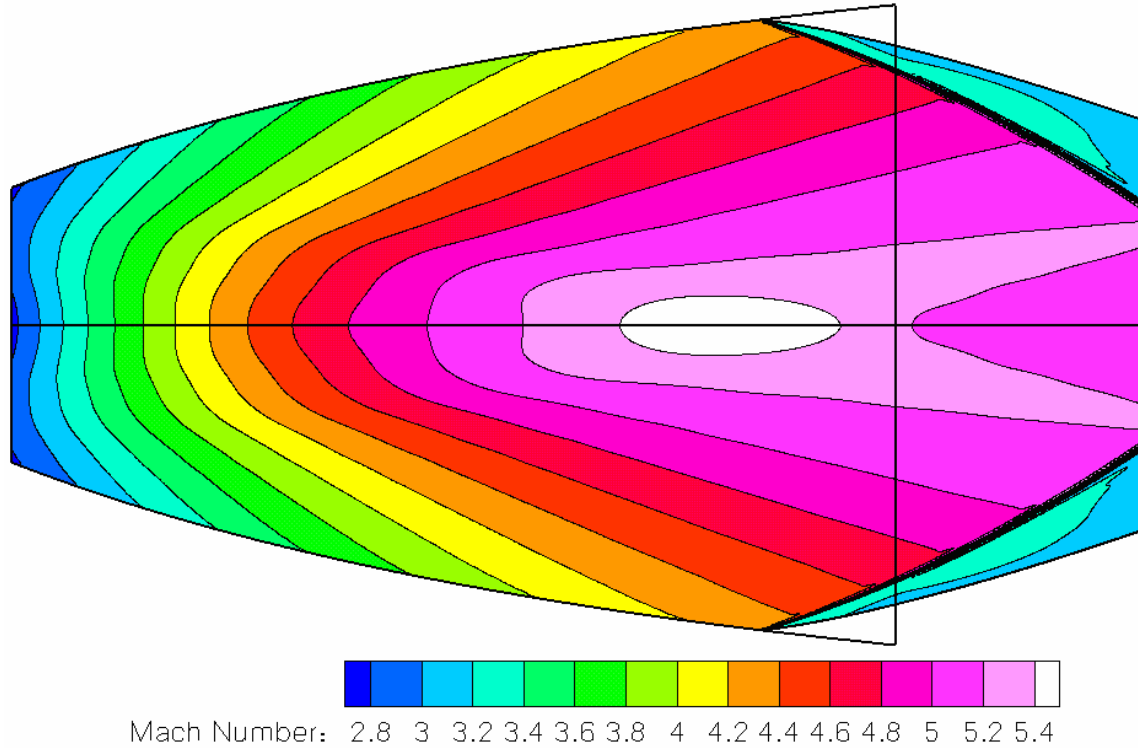


Figure 40: Mach number distribution in overexpanded Volvo S6 nozzle at $p_0=45$ MPa.

8.3 Calculations on the nonisobaric jet model

The calculations were performed on the Volvo S6 nozzle at the following conditions; $T_{0i}=450$ K, $p_0=4.5$ MPa, $\gamma_i=1.4$, $\mu_i=29$, $T_{0e}=300$, $p_a=100$ kPa, $\gamma_e=1.4$, $\mu_e=29$. The pressure distribution was calculated (method one) and compared with the experiment [38], see Figure 41. One can see that calculated pressure agrees badly with the experiment. Therefore were a study performed to find any possible errors in the model.

Focus was on the velocity ratio u_e^{**} since it has big influence on the pressure; see the similarity between Figure 41 and Figure 42 which shows the pressure ratio and velocity ratio u_e^{**} respectively. To compute the different velocities in the recirculation region several techniques were tested and evaluated, beginning with “calculation method 1”. As a first observation the initial condition of the pressure is too high. Lowering of this value requires the velocity ratio u_e^{**} to be less (more negative) then $(u_e^{**})_{\min}$, which is achieved when $y_w=y_e$ (Eq. (91)). Figure 43 illustrates the ratio between the calculated pressure gradients at the inner and outer boundary of the mixing layer. Since the pressure is assumed equal over recirculation region (y-dir), this ratio should be equal to unity. One can see that this is not the case and therefore another method was tested, i.e. “calculation method 2”. Since the velocities are derived from equal pressure gradients another test was

needed to check the method. The derivatives were in this case derived separately and therefore the velocities could be calculated in two separate ways; 1) with the velocity equation (Eq. (90)) and 2) with aid of derivatives, see Figure 44. However, it was found that this method did not give any further information. The velocities differed from each other and the velocity ratio u_e^{**} deduced from the derivative was bigger than zero at the nozzle exit. It should also be mentioned that the calculated pressure distribution (with calculation method 2) did not significantly differ from the calculated pressure (calculation method 1) in Figure 41.

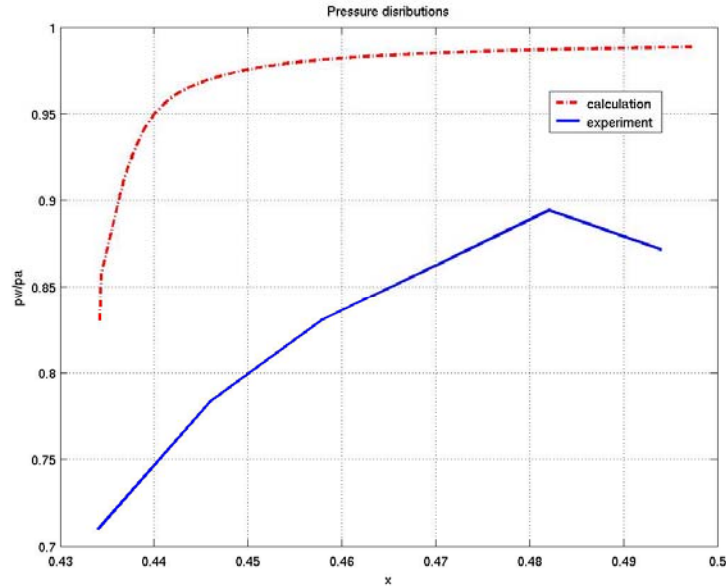


Figure 41: Calculated and experimental pressure distribution from separation point downstream the nozzle, Volvo S6 nozzle at 4.5 MPa operated with air

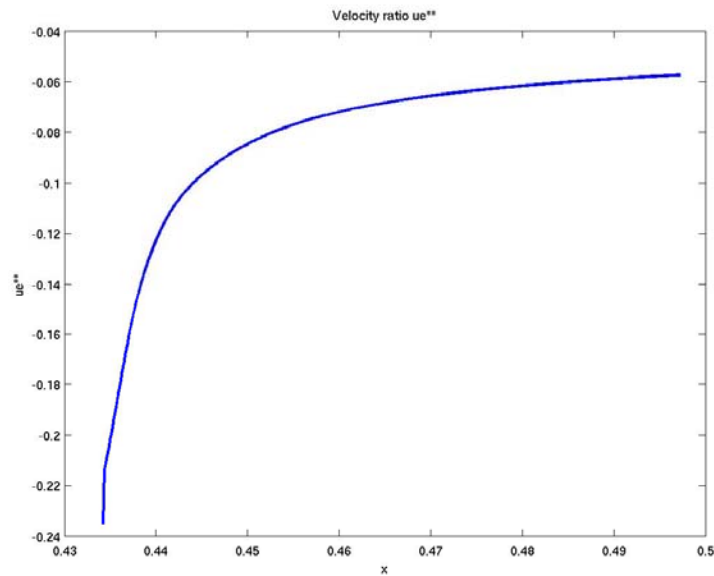


Figure 42: Velocity ratio u_e^{**} versus axial position

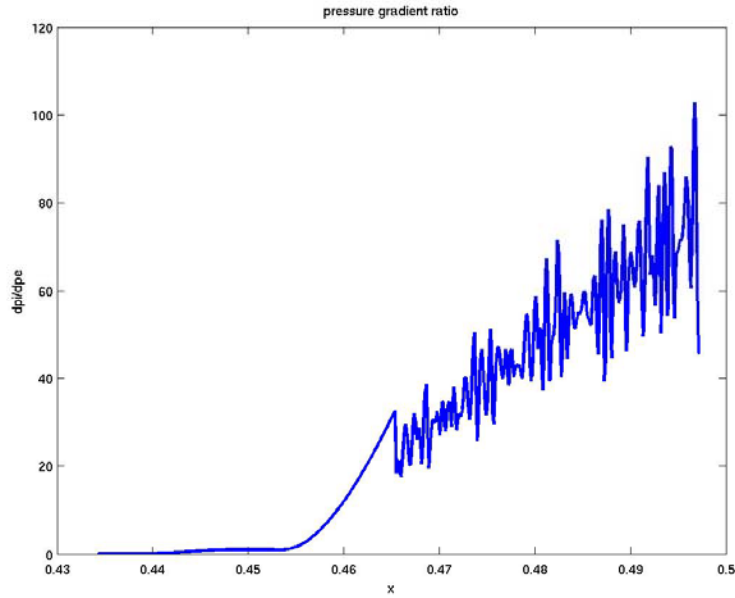


Figure 43: Pressure gradient ratio $\frac{dp_i}{dx} / \frac{dp_e}{dx}$ versus x

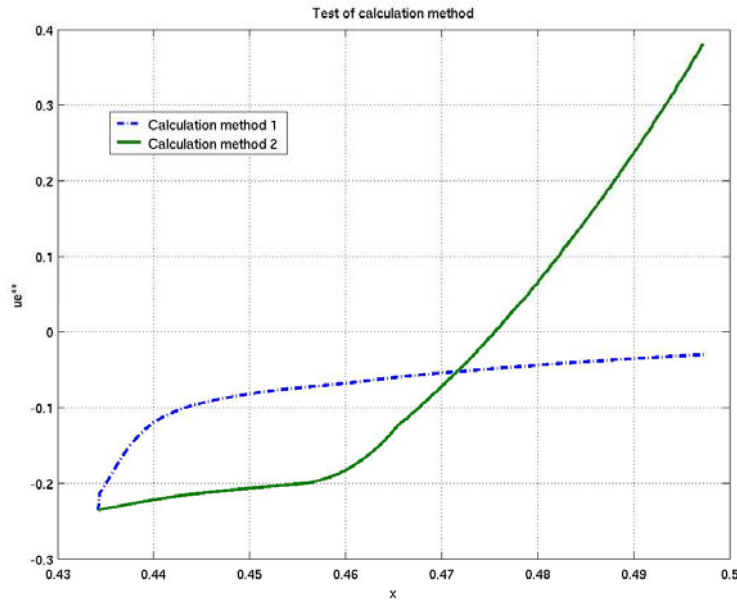


Figure 44: Comparison of u_e^{**} versus x

Finally a third method was tested, and it is a combination of the above methods. In the previous methods the velocity u_i at the inner boundary is collected from the ideal jet calculations. In this method it is derived from equal pressure gradients, i.e. same procedure as in Eq. (105)

$$\frac{1}{u_i} \frac{du_i}{dx} = \frac{\overline{\rho_e u_e^{**}} \frac{du_e^{**}}{dx} (1 + \tan^2 \theta)}{1 - \overline{\rho_e u_e^{**2}} \frac{(1 + \tan^2 \theta)}{(1 + \tan^2 \theta_i)}}. \quad (108)$$

A comparison of the velocity derived from Eq. (108) and the ideal jet is shown in Figure 45. The major difference between the two velocities is the gradient, which influences on the pressure gradient, see Eq. (52). Unfortunately it was found that this method did not significantly alter the calculated pressure profile. Since the different methods do not alter the obtained results, the velocity calculation method is eliminated as an error source.

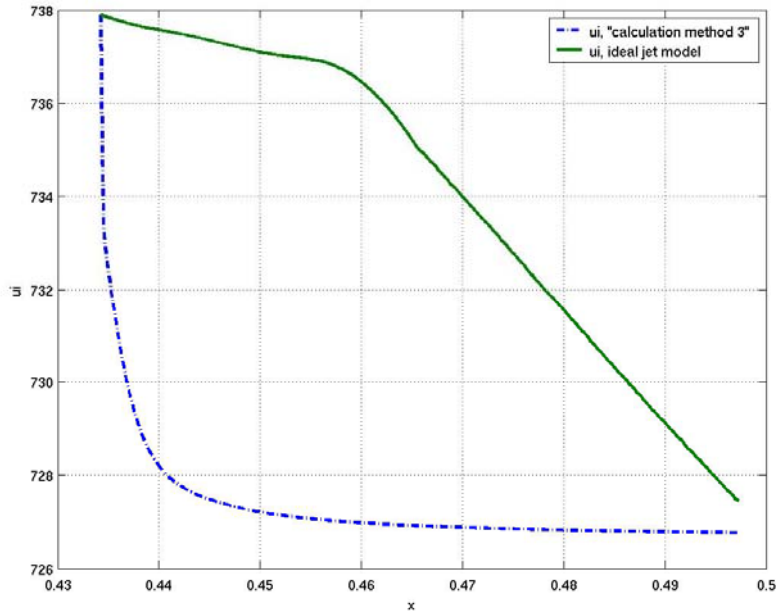


Figure 45: Comparison of different techniques to determine u_i

An additional test was performed by lowering the velocity ratio u_e^{**} below $(u_e^{**})_{\min}$ at the initial point. This did not affect the pressure distribution, only a small change at the vicinity of the initial point was observed. It can be explained by studying Figure 41, the velocity ratio u_e^{**} has a big gradient in that region and thus decreases $|u_e^{**}|$ rapid.

The “gradientless” model was also tested. It showed similar results as above, which means that the D term in Eq. (79) is the governed term. If we go back to Figure 31, it can be realized that the mixing growth is too big for large Mach numbers. A better fit to the experimental curve would be achieved if the mixing growth is less, i.e. multiplying D with a factor less than one for large Mach numbers. On the other hand, lowering the pressure can be made by multiplying D with a factor larger than one.

If we go back and look further on the pressure equation the density ratio ρ_e/ρ_i is the only factor which can influence the pressure besides u_e^{**} . Carefully checks were performed on the deduced equations but no error term was found. A further study of the model is therefore left to other workers.

9 Conclusion and outlook

This work presents the basic theory of flow separation and former semi-empirical flow separation models together with a new model for determination of the pressure- and flow distribution in the recirculation region.

Models reported in literature shows generally good agreement with performed experiments, however, they are only validated and developed for cold gases. Since rocket nozzles operate with hot gases, it is desirable to develop a model which include various parameters of the jet and ambient gas, which was the aim of this project. Studies have been performed to look at the feasibilities to extend the already existing models to also include for hot gases. The core in the models by Reijasse & Birkemeyer and Zerjeski is the Generalized Free Interaction Theory (GFIT), which is based on a physical model description of the SWBLI and not the viscous mixing process between the two different gas streams (which occurs after the nozzle flow has separated from the wall). Since no modeling of the flow is made in the recirculation region these two models can probably not be modified for hot propellants.

Malik & Tagirov's (M&T) model on the other hand is based on a theory for mixing of counter flowing turbulent jets in the recirculation region and therefore it is a promising model to be extended for hot gases. The new model is built on a similar approach and is an Integral method (developed to calculate mixing layer thicknesses in turbulent mixing flows), which includes the various jet and ambient gas parameters i.e.; Mach number just before the separation point, total temperature of the jet- and ambient medium gas, molecular weight of the jet and ambient medium gas, critical separation pressure ratio (off design pressure ratio), and nozzle contour in the separated zone. The new nonisobaric model is subdivided into two parts; an inviscid part which calculates the inviscid overexpanded jet shape and flow parameters by an Euler solver and a viscous part which uses the Integral method. The Euler solver also transforms the calculated jet to an equivalent homogenous ideal jet with the use of a flux averaging method.

The validation of the model was subdivided into three steps, i.e. comparison between calculated and experimental/published results of 1) the mixing of an isobaric jet, 2) the inviscid jet shape at off-design and 3) the mixing of a nonisobaric jet.

The validation of the isobaric mixing model was performed by studying the influence of jet Mach number, ambient medium velocity and total enthalpy on the initial length L_c . The calculations of the mixing layer for the isobaric jet agreed well with experimental data and physical discourses for the cases of the jet outflow into a still, co-flowing and counter-flowing ambient medium. The influence of total enthalpy was also taken into account correctly.

The calculations of the ideal jet shape showed good agreement with shapes from the literature for different Mach number, jet gas adiabatic exponent, nozzle wall angle and off-design pressure ratio. The deviation between the tabled and calculated shapes can be explained by the different techniques that are used in the calculation of the flow field upstream the separation. An additional test was also performed by comparing a calculation with experimental data (Schlieren photo) for a Volvo S6 nozzle test. It showed good consistency, which further strengthens the accuracy in the Euler solver.

As a last step, the two separate models were put together into the nonisobaric jet model and validated with experimental data for a Volvo S6 nozzle test. The predicted pressure showed poor agreement with the experimental pressure distribution. Extensive studies were performed to find the error or lack in the model, but no error was found. One way to improve the model might be to include some empirical corrections terms, similar to the one used in the model by Malik & Tagirov.

Once the model in the recirculation model was defined, the objective was to build a separation point prediction model. No time were spent on this, since the model in the recirculation region did not give satisfying results. But below are some suggestions on further works before a reliable separation point prediction model can be built.

Developing a new separation model demands additional work on the models in the interaction region, since they are not tested for hot gases. The iteration procedure which is used in the models by Reijasse & Birkemeyer and Zerjeski can not be used in a new model since the developed model in the recirculation region builds on momentum conservation, and is therefore always fulfilled. It is therefore proposed to develop a method that checks if the pressure ratio p_e/p_a is reasonable, and from there build an iteration procedure. A proposed separation model is a composition of four models; the boundary layer characteristics upstream the separation point, the model in the interaction region, the model in the recirculation region, and finally a model of the pressure ratio p_e/p_a .

In both the present and the models by Reijasse & Birkemeyer and Zerjeski the pressure are assumed to be constant over the recirculation region. CFD calculations show that the pressure is higher at the wall than at the inner boundary of the mixing layer. Therefore it is suggested to examine this slightly pressure rise further and try to find a simple model. The model may be as simple as a generalized ratio. The assumption of constant pressure is maybe the loss in Zerjeski's momentum calculations. Additional studies are also suggested to further examine the separation length and influence of wall temperature.

10 References

- [1] Östlund Jan, Supersonic flow separation with application to rocket engine nozzles, Technical report.
- [2] John D Anderson Jr, Modern Compressible Flow With Historical Perspective, second edition 1990, ISBN 0-07-001673-9.
- [3] Dr. Herman Schlichting, Boundary- Layer Theory, seventh edition 1979, ISBN 0-07-055334-3.
- [4] Alejandro L. Garcia. Numerical Methods for physics, second edition 2000 ISBN 0-13-906744-2.
- [5] Malina FJ (1940), Characteristics of the rocket motor based on the theory of perfect gases, Volume 230, J. Frankling Inst., 433-454.
- [6] Ahlberg J H, Hamilton S Migdal D and Nilson E N (1961), Truncated perfect nozzles in optimum nozzle design, ARS Journal, 31(5), 614-620.
- [7] Rao G V R (1958), Exhaust nozzle contour for optimum thrust, Jet Propulsion, 28(6), 377-382.
- [8] Zerjeski David, Semiempirisches Model zur Strömungsablösung in über-expandierenden Raketendüsen, Diplomarbeit Technische Universität Darmsatdt 2003.
- [9] Chapman D, Kuehn D and Larson H (1958). Investigation of separation flows in supersonic and subsonic streams with emphasis on the effect of transition, NACA Report 1536, Ames Aeronautical Laboratory, Moffet Field.
- [10] Erdos J and Pallone A (1962), Shock-boundary interactions and flow separation, Heat Transfer and Fluid Mechanics Institute Procs., Stanford University Press, Stanford.
- [11] Summerfield M, Foster C and Swan W (1954), Flow separation in overexpanded supersonic exhaust nozzles, Jet Propulsion 24
- [12] Schilling T W (1962), Flow separation in rocket nozzles, M. S. Thesis, University Of Buffalo, New York.
- [13] Crocco L and Probstein R (1954), The peak pressure rise over an oblique shock emerging from a turbulent boundary layer over a plane surface, Report 254, The James Forrestal Research Center, Princeton University, Princeton NJ.
- [14] Schumucker R (1973), Flow processes in overexpanding nozzles of chemical rocket engines (In German), Report TB-7, -10, -14, Technical University Munich, Munich
- [15] Lawrence R A (1967); Symmetrical and unsymmetrical separation in supersonic nozzles, PhD. Thesis, TX. Inst. of Technology, Southern Methodist University, Dallas.
- [16] Zukoski E E (1957), Turbulent boundary layer separation in front of a forward facing step, AIAA Journal 5(1)
- [17] Östlund J (2002) Flow processes in rocket engine nozzles with the focus on flow separation and side-load, Licentiate Thesis TRITA-MEK 2002:09, Department of Mechanics, Royal Institute of Technology, Stockholm, Sweden.
- [18] Frey M (2001), Behandlung von Strömungsproblemen in Raketendüsen bei Überexpansion, PhD. dissertation, Institut für Aerodynamik und Gasdynamik Universität Stuttgart, Stuttgart.
- [19] Carrière P, Sirieix M and Solognac J-L (1968), Propétiés de similitude des phénomènes de décollement laminares ou turbulents en ècoulmnt supersonne non uniforme, 12th International Congress of Applied Mechanics, Stanford University, Stanford, also ONERA TP N° 659F.

- [20] Kudryavtsev V M (1975), Fundamentals of theory and calculations of liquid rocket engines (In Russian), Moscow High School, Moscow.
- [21] Malik T and Tagirov R K (1988), A semi-empirical method for calculating separated turbulent flow in a conical Laval nozzle in the reexpansion mode (In Russian), Akademiil Nauk SSSR, Izvestiia, Meekhanika Zhidkosti I Gaza, 60-66
- [22] Reijasse and Birkemeyer J (2002), Semi-empirical flow separation model for subscale nozzles, Proc. 4th European Symp. Aerothermodynamics for space, Capua Italy.
- [23] Görtler H (1942), Berechnungen von Aufgaben der freien Turbulenz auf Grund eines neuen Näherungsansatzes, ZAMM, 22, pp. 244-254.
- [24] Benay R and Détery J, méthode de calcul de recollement d'un jet supersonique turbulent avec effets thermique, Onera report RT62/7078 AY.
- [25] Détery J and Sirieix M (1979), Ecoulements de culot, Onera report TP 1979-14 F.
- [26] Michael R (1963), Couches limites turbulentes et calcul pratique des couches limites en fluide compreeible. , Cours de 3^e année professé à l'Ecole Nationale Supérieure de l'Aéronautique.
- [27] Reshotko E and Tucker M (1957), Approximate calculation of the compressible turbulent boundary layer with heat transfer and arbitrary pressure gradient, NACA Technical Note 4154.
- [28] Papamoschou D (1988), The compressible turbulent shear layer; an experimental study, J. Fluid Mech. Vol 197, pp.453-477.
- [29] Brummund U and Scheel (2000), Characterization of a supersonic flowfield using different laser based techniques, 10th International Syposium, Applications of Laser Techniques to Fluid Mechanics.
- [30] Schlichting H and Gersten K (1997), Grenzschicht-Theorie, Springer Verlag, 9.Aufl, ISBN 3-540-55744-0.
- [31] Ginevsky A.S., Theory of turbulent Jets.
- [32] Anderson, Tannehill and Pletcher (1984), Computational Fluid Mechanics and Heat Transfer, ISBN 0-07-050328-1
- [33] Eckert E.R.G and Robert M. Drake Jr, (1987), Analysis of Heat and mass Transfer, ISBN 0-89116-553-3 or ISBN 3-540-17708-6
- [34] Lau J.C, Morris P.J and Fisher M.J (1979), Measurements in Subsonic and Supersonic Free Jets Using laser Velocimeter. Fluid Mech, v.93, part 1.
- [35] Morris P.J (1976), AIAA Journal, 14, 1976, pp.1468-1475
- [36] Ilizarova L.I and Ginevsky A.S (1962). Experimental Investigation of Jet in Counter-flow, in Industrial Aerodynamics, issue 23.
- [37] Averenkova G.I. and Ashratov E.A. el al. (1970), Supersonic Jets of Ideal Gas, Moscow State University, parts 1,2
- [38] Vulcan 2+, Campaign 6 test data, #2096-2099, 2101-2105,2107-2109, SV FIL 114 0000 E 2005, internal document.
- [39] Lars-Erik Eriksson (1994), Pressure loss evaluation by flux averaging, internal report
- [40] Lennart Råde and Bertil Westergren (1998), Mathematics Handbook for Science and Engineering, ISBN 91-44-00839-2

Appendix 1: Prediction iteration process

